MIDLATITUDE EXTREME WEATHER IN AN IDEALIZED CHANGING CLIMATE

A Dissertation

Presented to the Faculty of the Graduate School

of Cornell University

in Partial Fulfillment of the Requirements for the Degree of

Doctor of Philosophy

by

David Burrows

January 2017

MIDLATITUDE EXTREME WEATHER IN AN IDEALIZED CHANGING CLIMATE

David Burrows, Ph.D.

Cornell University 2017

The relationship between the midlatitude eddy-driven jetstream and extreme atmospheric phenomenon, such as blocking anticyclones, atmospheric rivers, droughts, floods, and more, motivate concern from the meteorological and climate community to the general public and policy makers. Poleward or equatorward shifts in the jetstream may persist for a week to nearly a month, emerging as the leading mode of midlatitude dynamics and weather. The persistence that the north-south fluctuations in the jetstream contains is standardly analyzed through principal component analysis, where the leading mode of variability is the shift in jet latitude of the jetstream and is referred to as the annular modes, or zonal index. Comprehensive climate models have been shown to exhibit biases in the time scales associated with the annular modes. This is attributed to biases in climatological jet latitude, with important implications for projections of future climates and midlatitude weather events. Specifically, equatorward biases lead to the modeling of overly persistent jet shifts leading to erroneous projections into future climates.

The eddy-mean flow interaction that characterizes the persistent anomalous state of the midlatitude jet depends on processes associated with the lower-tropospheric source of vertically propagating Rossby waves and processes associated with upper-tropospheric wave propagation and breaking. Although these mechanisms will not be explicitly detailed in this thesis, more details on

the effect that different physical processes has on the annular mode time scales and eddy-mean flow feedbacks can be found in [17]. Instead, the effect of model resolution and truncation will be analyzed in the Geophysical Fluid Dynamic Laboratory's dry, atmospheric model to find consistencies across different grid configurations. A variety of climate change-like thermal forcings are used to generate a range of meridional shifts in the midlatitude eddy-driven jet. These thermal perturbations are used to mimic idealized greenhouse gas warming and El Niño/Southern Oscillation variability, both of which increase the equator-to-pole temperature difference (ΔT), and Arctic amplification (AA) which reduces ΔT. This produces a range of jet latitudes with which to examine annular mode variability. It is shown that along with a decrease in the time scales of jet variability, there is also a reduction in the eddy momentum feedback strength with an increase in jet latitude. These results are in agreement with many other modeling efforts including phase 3 and phase 5 of the Coupled Model Intercomparison Project.

Recent proposals linking AA to increases in extreme events have received scrutiny from the scientific community for the lack of dynamical insight. It is believed that the reduction in ΔT leads to a less meridionally confined, amplified jetstream leading to enhanced advection of heat (cold or warm) and moisture. With an enhanced persistence, these events can lead to extreme weather. To test this hypothesis further ΔT can be directly increased (polar cooling) or decreased (polar warming) in a highly idealized model to determine the effect on midlatitude dynamics and extreme weather. Two methods will be used to define a blocking anticyclone and to classify isolated extreme weather events. Classically, blocking describes persistent, large amplitude, Rossby wave breaking in the middle to high latitudes leading to midlatitude easterlies and stalled

weather systems. It will be shown that by decreasing ΔT, the midlatitude jetstream weakens and shifts equatorward along with eddy fluxes of heat and momentum. Following this, the blocking response shifts equatorward and weakens indicating a reduction in persistent blocking patterns. The climatological finite amplitude wave activity also reduces at all latitudes. These results are corroborated by using a more subjective definition of extreme events and show that the AA hypothesis does not hold true for this idealized model.

BIOGRAPHICAL SKETCH

My name is David Burrows. I was born in Opelika, Alabama, where as a child I became immensely fascinated with weather especially thunderstorms and tornados. After receiving a foot of snow in southern Alabama from the blizzard of '93, my family and I moved to Syracuse, New York, (the lake effect snow capital of the world) where I was raised. My second great passion of math came in my years of highschool, particularly a math teacher at Fayetteville-Manlius highschool, Mr. Stedman. Having developed a passion for math, I entered Castleton State College (now Castleton University) in 2006 to earn a bachelors of art in mathematics in 2009. In the process of filling out applications to enter graduate school for math, I realized how boring of an existence it would be to study theoretical math the rest of my life. I threw away my applications and instead applied for another undergraduate degree in meteorology. With a few options for undergraduate school, I chose the Metropolitan State College of Denver (now the Metropolitan State University of Denver) where I completed introductory classes in meteorology, Synoptic, Climate, Radar, and Instrumentation. This set me up to apply for graduate school and was accepted to study at Cornell University under my advisor Gang Chen. I completed my masters in 2013 and continued on with doctoral research. This thesis is a culmination of this doctoral research.

The family.

ACKNOWLEDGEMENTS

I want to acknowledge the EAS community at Cornell University, particularly my research group whose weekly meetings helped broaden my interest in atmospheric dynamics. Specifically, I want to thank Doctors Stephen Colucci, Lantao Sun, Mike Kelleher, Huang Yang (Caesar), and Daniela Domeisen as well as my committee member Doctors Natalie Mahowald, Peter Diamessis, and Peter Hess. I also acknowledge the 2011 through 2016 undergraduate, atmospheric community who alllowed me to practice and develop my teaching skills and Mark Wysocki for interesting conversations and always providing a laugh. I mostly want to acknowledge my advisor, Doctor Gang Chen, who gave me the tools, advice, and support needed to make it through the long journey of graduate school.

TABLE OF CONTENTS

Biographical Sketch . . . iii
Dedication . . . iv
Acknowledgements . . . v
Table of Contents . . . vi
List of Tables . . . vii
List of Figures . . . viii

1 Introduction **1**
1.1 General Circulation . . . 1
1.2 Midlatitudes . . . 3
1.2.1 Annular Modes . . . 4
1.2.2 Persistent Wave Events . . . 7
1.3 Outline . . . 8

2 Model and Wave Activity **10**
2.1 Model Configurations and Perturbations . . . 10
2.1.1 Tropical Tropospheric Warming (TTW) . . . 14
2.1.2 Tropical Upper-tropospheric Warming (TUW) . . . 17
2.1.3 Arctic Surface Warming/Cooling (ASW/C) . . . 17
2.2 Finite-Amplitude Wave Activity . . . 19
2.3 Summary . . . 21

3 Annular Mode Time scales **22**
3.1 Method . . . 22
3.2 Results . . . 30
3.3 Summary . . . 34

4 Extremes **37**
4.1 Method . . . 40
4.2 Results . . . 44
4.3 Summary . . . 51

5 Blocking **52**
5.1 Method . . . 52
5.2 Results . . . 57
5.3 Summary . . . 59

6 Conclusion **60**
6.1 Discussion . . . 62
6.2 Future Work . . . 68

Bibliography **70**

LIST OF TABLES

2.1 A list of the numerical values used in the thermal perturbation runs. For the TTW and TUW runs, the parameters in Eq. (2.1) are altered: $F(p)$ and $W(\phi, \phi_0)$ set the vertical and meridional structure of the heating, where ϕ_0 is the latitudinal width of the warming perturbation and $\delta\phi = 5°$ sets the meridional sharpness of the thermal perturbation boundary. For the ASW/C runs, an additional heating rate is specified by $\frac{\partial T}{\partial t}|_{ASW/C}$ with $F(p) = 0$. For all the runs, A_0 is the magnitude of the heating, and p_0 is 1000hPa. Notice the ASW have positive A_0, and ASC have negative values. All the simulations are run at the R30 resolution, and the bold numbers in TTW indicate the simulations conducted at R60, T42, and T85 resolutions. 11

LIST OF FIGURES

1.1 Schematic depicting the large-scale general circulation features on Earth. L stands for low pressure or low heights, and H stands for high pressure or high heights. Lines with arrows indicate the direction of the surface flow with easterlies in the tropics, westerlies in the midlatitudes, and eastlerlies in polar regions. The white cloud looking features in the equatorial regions represent regions of deep convection. The circulation features on the left side of the figure represent the vertically rotating cells. All other features are identified in the figure. 2

2.1 Responses in temperature (shades with a 2 K interval) and zonal-mean zonal wind in m s^{-1} (black contours) between ΔT runs and the control run for (a) ΔT = 40 K, (b) ΔT = 50 K, (c) ΔT = 70 K, and (d) ΔT = 80 K. Dashed contours are negative, and the vertical gray line in each plot indicates the climatological jet latitude for the control run. 13

2.2 Same as Fig. 2.1 but also includes the response in the radiative-equilibrium-temperature profiles (green contours at 4 K, 8 K, and 12 K) for (a,b) tropical tropospheric warming (TTW) runs, (c,d) tropical upper-tropospheric warming (TUW) runs, and (e,f) Arctic surface warming and cooling (ASW/C) runs. For the TTW and TUW runs, 10° wide runs are in the left column, and 30° wide runs are in the right column. For the ASW/C runs, the left column is warming, and the right column is cooling. Each forced run uses the quadrupled value of A_0 which shows the biggest forced response. 16

2.3 Climatological jet latitude as a function of forcing strength for (left) tropical temperature warming (TTW) runs, (middle) tropical upper-tropospheric warming (TUW) runs, and (right) Arctic surface warming/cooling (ASW/C) runs. Closed circles indicate broad warming runs (e.g. ϕ_0 = 30°) for the TTW and TUW runs (left and center) and also for ASC runs (right) (e.g. negative values of A_0). 20

3.1 Top panel: the zonal index (leading principal component time series of the vertical- and zonal-mean zonal wind) as a function of model day. Middle panel: daily jet latitude (calculated as the latitude at which the climatological jetstream maximizes at the 850 hPa level) as a function of model day. Bottom panel: scatterplot of the daily values of the zonal index and the jet latitude. . . 23

3.2 Control run climatology (contours) and lag 0 regressions onto the zonal index (shades), representing the leading mode of variability, for (a) zonal-mean zonal wind and (b) eddy momentum flux convergence and Eliassen-Palm vectors. Negative contours are dashed. The contour intervals for the regression in (a) are 0.5 m s^{-1} and (b) are 0.2 m (s day)$^{-1}$. Climatology contour intervals are indicated in the figure. (c) Lagged autocorrelation of the zonal index from Fig. 3.1. The horizontal dashed line is the value of the *e*-folding time scale. 25
3.3 Control run lagged-regressions onto the zonal index for (a) zonal-mean zonal wind (m s^{-1}) vertically averaged from 1000 hPa to 100 hPa and (b) eddy momentum flux convergence (m s^{-1} day^{-1}) vertically averaged from 500 hPa to 100 hPa. Negative lags indicate eddy-time series lead the zonal index, while positive lags the zonal index leads. Negative contours are dotted. The horizontal gray line in each plot indicates the climatological jet latitude. 26
3.4 Control run eddy momentum flux convergence of (a) the lagged covariance of eddy time series in Eq. (3.3) onto the zonal index (units: (m s^{-1})^2 day^{-1}) and (b) feedback strength. Vertical lines in (b) indicate the 95% confidence intervals based on 1,000 bootstraps (see text for calculation details.) 28
3.5 R30 truncation: (a) Zonal index lagged-autocorrelation (only positive lags shown). The horizontal black dashed line indicates the *e*-folding time scale. (b) *e*-folding time scale as a function of climatological jet latitude. (c) Lagged-covariance of m_{up} in (3.3) with the zonal index for positive lags when zonal index leads m_{up}. (d) Eddy momentum flux convergence feedback strength, b_{up}, as a function of positive lag. The colorbar, marker colors, and line colors for all plots indicate the latitude of the jet with warmer (red) colors for equatorward jet latitudes and cooler (blue) colors for poleward jet latitudes. Black lines and shapes represent the control run. Shapes for (a,c,d) are indicated in (a), and shapes for (b) are indicated in (b) with non-filled shapes representing narrow warming runs and filled shapes representing broad warming runs. 32
3.6 Eddy momentum feedback streghth, b_{up}, averaged over lags +10 to +18 days as a function of jet latitude. Colors are the same as Fig. 3.5. Black line is a linear best fit line. Error bars are computed from 1000 iterations using the bootstrap method; see text for more details. 33

3.7 As in Fig. 3.5, except that the diagnostic is applied to different horizontal resolutions and truncations. In all the plots, open circles indicate the narrow tropical tropospheric warming (TTW) runs, closed circles indicate the broad TTW runs, and diamonds indicate the control runs for each resolution including R30, R60, T42, and T85. Experiments with the standard heating and quadruple heating are used (see bold numbers in Table 2.1). In (b), data points are not color coded by jet latitude, as in (a), (c), and (d), but are color coded by their resolution and truncation as indicated by the legend. 35

4.1 An illustration of the extreme event definition presented in [32] for a positive extreme event (top row) and negative extreme event (bottom row). An event is defined to occur on day t_0 in the middle column and day $t_0 - 2$ to $t_0 + 2$ are also shown across each row. Within each panel, the shades are the time-mean T850 anomalies (2 K contour interval), black horizontal contour is the climatological jet latitude, black box represents the 30° latitude-by-longitude box used to define an extreme event (see text for details). The subtle green dots throughout the domain show where other extreme events are occuring. 39

4.2 R60 control run mean extreme event statistics. Top row is the average number of events occuring at a particular grid point over a 100 day period for warm (left) and cold (right) extreme events. The contour interval and units for the top row are 2 events per 100 days. The bottom row shows the zonal average of the top panels for warm (red) and cold (blue) extremes. The climatological jet latitude is also plotted in all panels as a black contour. . . 40

4.3 850 hPa temperature (T850) statistics (described below) as line plots in the left column and a shaded plot in the right column. For the right column, each experiment's statistic as a function of latitude is placed at its jet latitude along the x-axis with physical latitude as the y-axis and extrapolated to form a contour plot. The colors of the lines in the left column and x's in the right column indicate the experiment with red for ΔT = 40 K and blue for ΔT = 80 K. Black lines and diamonds represent the control run (ΔT = 60 K). The first row, (a) and (b) is the time- and zonal-mean T850 in K; the second row, (c) and (d), is the meridional gradient of the first row (T850) in K(100 km)$^{-1}$; the third row, (e) and (f), is zonal-mean standard deviation of T850; and the fourth row, (g) and (h), is the zonal-mean skewness of T850 in K. The thin black lines in the right column indicate the one-to-one line for physical latitude and jet latitude. The contour intervals for (b) are 5.5 K, (d) 0.3 K(100 km)$^{-1}$, (f) 2 K and (h) 0.4 K. 43

4.4 The extremes statistics are shown in a similar fashion to Fig. 4.3 with each experiment shown as a contour in the left column and shaded in the right column. Positive extremes are in the top row with negative extremes in the bottom row. Experiments are again stacked at the latitude of the jetstream in the right panel. Colors, markers, and lines are described in Fig. 4.3. The units for the right column are number of events per 100 days with a contour interval of 1.6 events per 100 days. 46
4.5 Same as Figure 4.4 but the tropical-temperature warming (TTW) runs have been added (see Table 2.1 for details). The TTW runs are added as circles, and the markers and lines are colored by jet latitude, redder lines for equatoward jets and bluer lines for poleward jets. Open circules are the narrow TTW runs, and filled circles are the broad TTW runs. The units for the right column are number of events per 100 days with a contour interval of 1.6 events per 100 days. 48
4.6 Same as Figure 4.5, but the lines in the left column and the experiments in the right column are ordered by jet speed with faster jets in blue and slower jets in red. The maximum in the latitudinal distribution of extreme events are all stacked near 45°. Note the broad TTW runs are not filled here for figure clarity. The units for the right column are number of events per 100 days with a contour interval of 1.6 events per 100 days. 49

5.1 The 7 day evolution of a blocking anticyclone as defined in [42] and described in the text. Day t_0 represents the first day that a particular grid point was marked as blocked. The black contours are the Z500 field; shades are time- and zonal-mean Z500 field that has been normalized by the latitudinal maximum in the zonal-mean standard deviation of Z500 (contour interval of 0.4 m); pink contours is the same field but marking when it exceeds a certain sigma value (B matrix in text), 1.5 sigma here; red contours delineate large-scale reversal in the Z500 field. 54
5.2 Same as Figure 4.2 but for the 500 hPa geopotential height (Z500) statistics using the blocking algorithm from [42]. Blocking frequencies are presented as the percentage (%) of time that a particular point (left panel) is considered blocked and the zonal mean of this quanity (right panel) as the percentage of days that a particular latitude is considered blocked. 55
5.3 Same as Figure 4.3 but for the 500 hPa geopotential height (Z500) statistics. The contour intervals and units for (b) are 80 m, (d) 4 m $(100\text{km})^{-1}$, (f) 24 m and (h) 0.3 m. 56

5.4 The block response is shown in a similar fashion to Fig. 5.3 with each experiment shown as a contour in the left column and shaded in the right column. Colors, markers, and lines are described in Fig. 5.3. 58

6.1 (a) Time-mean finite-amplitude wave activity, A, as contour plots for each ΔT run and (b) a shaded plot that combines each experiment as a function of physical latitude and experimental jet latitude. Markers and colors are the same as Fig. 4.3. 63

6.2 Top row: the amplitude of the maximum value of the T850 meridional gradient (dTdy) (left panel) and latitude of this maximum value (right panel) as a function of climatological jet latitude. Bottom row: the same T850 gradient values but as a function of jet speed. Markers and colors are the same as Fig. 4.3. Correlation coefficients are shown as floating numbers for each respective panel. 64

6.3 Same as Fig. 6.2 but the tropical temperature warming (TTW) runs have also been added. Colors have been removed. Circles represent the TTW runs, x's the ΔT runs, and the diamond is the control run. Closed circles indicate the broad TTW runs. 65

6.4 Same as Fig. 4.6 but for the R30 simulations. Included in the plots are the tropical temperature warming (TTW) runs (circles), the tropical-upper tropospheric (TUW) runs (triangles), the Arctic surface warming/cooling (ASW/C) runs (stars), and the ΔT runs (x's). For figure clarity, the broad TTW and TUW runs have not been filled. The contour interval and unit for the right column are 2 events per 100 days. 67

CHAPTER 1

INTRODUCTION

1.1 General Circulation

The large-scale general circulation of the atmosphere, generated through the unequal meridional heating of a rotating, spherical Earth and depicted in Fig. 1.1, necessitates mechanisms to transport the excess of heat from the equatorial regions. In the tropics, a thermally direct Hadley circulation removes heat from the equatorial regions with surface easterlies throughout the tropics and an upper-level, westerly jet (angular momentum conservation) in the subtropics. The down-welling branch of the Hadley circulation pattern coincides with the subtropical dry zones. In midlatitude regions where poleward flowing warm, moist air and equatorward flowing cool, dry air converge, the strong baroclinic zones generate a westerly jetstream.

With the imminent advance of large-scale climate change, concern rises over the evolution of the general circulation in the future. The climate system's response due to greenhouse gases (GHG), such as carbon dioxide (CO2), may take many years to fully reveal itself, as the oceans take time to absorb and release the additional heat added into the climate system, as well as the long-lived nature of CO2. In general, from the Clausius-Clapeyron relation, the water vapor holding capacity increases with rising temperatures, leading to more intense and extreme precipitation events [96, 47]. As the mean temperature on Earth changes, the general circulation and its dynamical constituents displays a poleward shift in both the Hadley circulation e.g. [61, 83] and the midlatitude jetstream and storm tracks [100, 55, 22, 58]. It is thus essential to understand the general circu-

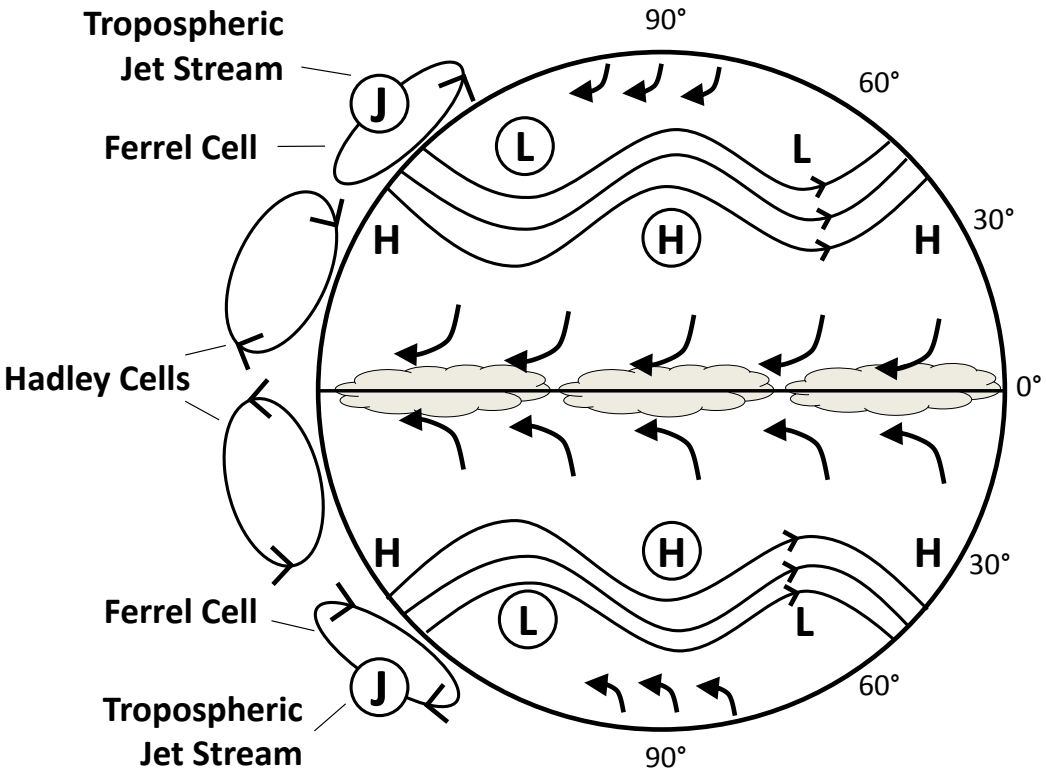

Figure 1.1: Schematic depicting the large-scale general circulation features on Earth. L stands for low pressure or low heights, and H stands for high pressure or high heights. Lines with arrows indicate the direction of the surface flow with easterlies in the tropics, westerlies in the midlatitudes, and eastlerlies in polar regions. The white cloud looking features in the equatorial regions represent regions of deep convection. The circulation features on the left side of the figure represent the vertically rotating cells. All other features are identified in the figure.

lation's response to climate change and how heat and moisture transport may have been or may be altered in a past or future climate.

1.2 Midlatitudes

Focusing on the midlatitudes, the jetstream exhibits multiple time scales of variability that describes the north-south fluctuation of the jetstream on the hemispheric scale [94]. On a daily time scale, the variability of this jetstream is intimately related to the sensible weather in the midlatitudes, such as rainstorms, snowstorms, thunderstorms, and more, most prevalent in the preferred storm tracks downstreams of the continents in the Northern Hemisphere [45]. On a subseasonal to seasonal time scale, the jetstream, on average, may contain persistent anomalies where the jetstream and associated weather patterns are shifted poleward or equatorward of their climatological positions [45], such as the North Atlantic Oscillation pattern. This persistence is an eddy momentum feedback on the jet shift that prolongs the north-south shift. The zonal jet vacillation and its associated eddy feedback are important for stratosphere-troposphere coupling and tropospheric predictability [2, 33], tropospheric blocking patterns [99], Rossby wave breaking e.g. [13, 31, 87], and the extratropical circulation responses to El Niño [52, 22] and ozone depletion [38, 71, 86]. Although the annular modes describe a hemispheric scale of variability, regional jet variability also exists and is related to features in midlatitude dynamics such as persistent wave events or blocking.

This paper will focus first on the hemispheric scale variability associated with the annular modes, then turn to the regional scale of variability associated with wave events such as blocking anticyclones and persistent cyclones. These high amplitude anticyclone events are linked to extreme weather such as cold air outbreaks in Tibet [90] and the eastern half of the United States in January 2014 [80], steering of post-Hurricane Sandy into the East Coast of the United

States [8], 2003 heat wave and drought in Europe [14], and the 2010 Russian heat wave [27, 66]. These events are associated with persistent blocking-like patterns that lead to large-scale advection of either cold or warm temperatures, or persistent steering in the case of Sandy, for an extended period of time underlying the importance of blocking to midlatitude weather and extremes. Poor air quality also results from stagnant weather patterns and large-scale subsidence associated with the high pressure systems [92]. Thus, it is highly important from the research community to the public to the policy makers to understand how blocking or large amplitude events may change in future climates and their relationship to extreme weather events. The following two sections will describe current research associated with the annular modes and persistent wave events.

1.2.1 Annular Modes

The north-south fluctuation of the midlatitude jetstream about its climatological position, also known as the zonal index, describes the leading mode of extratropical atmospheric variability [94]. Because there is a link between jetstreams, sensible weather, and extreme weather events, it is essential to understand the trends in the zonal index to determine which latitudes or regions may be impacted by global climate change, e.g. [43]. Particular focus in the literature has been given to the response of midlatitude dynamics to Arctic amplification (AA). AA describes the unequal heating of the globe, from global warming, due to the melting of the Northern Hemisphere's sea-ice which will accelerate heating in the high latitudes compared with the midlatitudes or equatorial regions. The effect reduces and shifts temperature gradients across the midlatitudes affecting jetstream variability and has led to contradicting viewpoints as to the

midlatitude's dynamical response in observations [30, 53, 91] and in modeling efforts [42, 32]. With the context of these conflicting viewpoints of the midlatitude's response to climate change, this paper focuses on modeling the midlatitude's response to idealized climate change by shifting the latitude of maximum baroclinicity and/or changing the magnitude of the baroclinic zone.

Observations show a trend toward the positive phases, or poleward shift, of the Northern and Southern annular mode with time [94, 93, 63]. Modeling studies have confirmed that the response to GHG forcing [49] and ozone depletion [38] induce this poleward shift in the midlatitude jetstream system, whereas the response to ozone recovery is an equatorward shift consistent with a contraction of the Hadley circulation [86]. These results are confirmed with integrations from the Intergovernmental Panel on Climate Changes (IPCC) fourth assessment report [61, 83, 100, 55], other climate models [22, 58] and Phase 5 of the Coupled Model Intercomparison Project (CMIP) models [7] demonstrating a poleward shift of the general circulation. As these modes of jetstream variability coincide strongly with distributions of Rossby wave breaking [13, 31], which influence the characteristics of atmospheric rivers and blocking events [13, 64, 87, 39, 68, 77], subseasonal to seasonal variability is essential to reveal the midlatitude's response to climate change.

The zonal jet variability can be simulated in a wide variety of models from quasigeostrophic models [50, 101] to idealized primitive equation models [36, 21] to comprehensive general circulation models [34, 5]. While the spatial structure of a meridional shift in the jet is well understood, the time scale associated with the jet shift is more complicated and warrants further inspection due to its implication for predictability and climate sensitivity [37]. The annu-

lar mode, or shift in the midlatitude jet, is well described by the vertical- and zonal-mean zonal wind that is driven by eddy momentum forcing and damped by friction [21]. The associated eddies contain power in short time scales that rapidly initiate an annular mode response and power at longer time scales that maintain a shifted jet [56]. This low-frequency variability of the eddy momentum flux sustains a zonal wind anomaly against frictional damping, and this contributes to the persistent zonal wind anomaly associated with the annular modes [29, 76, 36, 40, 54].

Even as models become ever more complex, including coupling between biogeochemistry processes, atmospheric dynamics, oceanic feedback, and more, they still experience biases in the large-scale mean state of the atmosphere leading to other biases related to atmospheric dynamics. Nearly fifty years after first simulating the midlatitude variability [62], phase 3 and 5 of CMIP still produce biases in the mean state jet system, which is often simulated equatorward of its observed location [48, 89]. This equatorward bias has at least two main implications. [37] has shown that this bias in jet latitude manifests itself into an overly persistent midlatitude jet system. The forced response relating to climate change in phase 3 of CMIP also displays greater sensitivity for jets biased equatorward [48]. The dynamical consequence may lead to erroneous conclusions relating to the large-scale modes of variability, blocking, atmospheric rivers, and Rossby wave breaking that are essential to midlatitude dynamics and their associated extremes. Recent work [59] demonstrates that models with resolutions approaching 50 kilometers are able to simulate the observed midlatitude jetstreams location and intensity. Similarly, more realistic statistics with increasing model resolution for blocking [67, 46], atmospheric rivers [97, 25], and internal mode variability[37, 1] have been identified. This demonstrates that midlatitude

variability may suffer from low resolution models, so this analysis will discuss time scales of jetstream variability with two different truncations and two different resolutions (one high and one low). Chapter 3 will be dedicated to further modeling efforts and discuss the sensitivity of model resolution and truncation to annular mode time scales.

1.2.2 Persistent Wave Events

First defined in [73, 74], large amplitude anticyclones can develop in the midlatitudes which may reverse the westerly jetstream leading to stalled weather systems, especially over the North Atlantic and North Pacific. Slow moving weather systems make up a large part of the climate system and are shown to be associated with extreme weather events such as cold air outbreaks [90, 80], heat waves and droughts [14, 27, 66] and air quality issues [92].

Owing to this relationship between blocking and extreme weather events and its relationship to a large part of climate-related damage [43], it is essential to understand the response of persistent wave events, or blocking, to climate change. Blocking statistics are sensitive to blocking detection algorithms, observational datasets used, and time periods used for the analyses which may mask recent observations of trends in blocking statistics [7, 24]. As mentioned above, recent studies suggest that declining sea-ice over the Arctic regions has led to an increase in blocking across the Northern Hemisphere due to the reduction in north-south temperature gradient and a slowdown in the midlatitude flow [53, 30]. However, models in both phase 3 [10] and phase 5 [9] of CMIP agree that while a slight seasonal dependence on blocking occurs, a general decrease

in blocking for future climates is expected, contradicting [53, 30]. Two distinct modeling methodologies also showed that with idealized AA, a reduction in the number of extreme events occurs [42, 32]. With the controversary in the literature, a hierarchical approach with a highly idealized numerical model is warranted to determine the midlatitude response to idealized climate change.

This paper will initially test the midlatitude's response in terms of extremes and blocking events to a highly idealized AA signature. It will be shown that the results from [42] and [32] can be recovered if the model is ran at a sufficient resolution and for a sufficient length of time. The results will then be extended to generalize the AA results to different types of idealized global climate change. It will be shown that an increase in jet latitude does correspond to an increase in extreme events, but it will also be shown that an increase in jet speed also leads to an increase in extreme events. Two studies were able to remove the dependence on jet speed, and thus isolate the effects of jet latitude [42, 32], giving similar results to a subset of the experiments considered here, which include changes in both jet speeds and latitudes.

1.3 Outline

The outline of the thesis is as follows. Chapter 2 introduces the idealized model used throughout the study. The climate change-like thermal perturbations and the mean state response, e.g. the temperature and wind profiles, are also discussed. Chapters 3, 4, and 5 describe the annular mode response, extreme event response, and blocking response to idealized climate change, respectively, and will all begin with that chapter's methodology followed by results. Each chap-

ter will conclude with a brief summary of the main points presented in that chapter. Chapter 6 will synthesize the results presented throughout this study, discuss its significance in the current literature, and provide details of future work that could be conducted. The copyright of the content in Chapter 2 and Chapter 3 has been transferred to the American Meteorological Society.

CHAPTER 2

MODEL AND WAVE ACTIVITY

2.1 Model Configurations and Perturbations

Recent studies hypothesize that the north-south meandering of the midlatitude, eddy-driven jetstream and associated weather patterns may increase as the Arctic regions heat faster than the midlatitude and equatorial regions (known as Arctic Amplification - AA hereafter), thus decreasing the midlatitude-to-pole temperature difference [53, 30]. However, using an idealized dry model, [42] have shown that with a decrease in the equator-to-pole temperature difference, ΔT, the opposite is true. When a decrease in ΔT is forced, Fourier decomposition suggests a robust decrease in meridional wave amplitudes and related blocking statistics. Using an idealized dry model, [32] have shown that an equatorward shift of the jetstream (without changing the jet speed) leads to a reduction in the number of extreme events, which again is inconsistent with the AA theory. Following this hierarchical approach, various thermal perturbations are used to mimic global climate change in an idealized model configuration to deduce the response of the midlatitude jetstream dynamics.

The Geophysical Fluid Dynamics Laboratory (GFDL) dry atmospheric dynamical core is used to take advantage of its physical simplifications (e.g. no water, topography, seasonal cycle or diurnal cycle). Following [44], the control run is driven by a relaxation toward a zonally symmetric radiative-equilibrium-temperature profile with linear frictional damping in the planetary boundary layer. Climate change-like thermal perturbations allow a systematic shift of the climatological jet, either equatorward or poleward of the control run. A rhom-

Experiment Description	ϕ_0	A_0
Tropical Tropospheric Warming (TTW)	$10°, 30°$	-0.015625
$F(p) = A_0$	$10°, 30°$	-0.03125
$W(\phi, \phi_0) = 0.5\{1 - \tanh[(\lvert\phi\rvert - \phi_0)/\delta\phi]\}$	**$10°$, $30°$**	**-0.0625**
	$10°, 30°$	-0.125
	$10°$, $30°$	**-0.25**
Tropical Upper-Tropospheric Warming (TUW)	$10°, 30°$	-0.015625
$F(p) = A_0 \exp\left[-(p/p_0 - 0.3)^2/(2 \times 0.11^2)\right]$	$10°, 30°$	-0.03125
$W(\phi, \phi_0) = 0.5\{1 - \tanh[(\lvert\phi\rvert - \phi_0)/\delta\phi]\}$	$10°, 30°$	-0.0625
	$10°, 30°$	-0.125
	$10°, 30°$	-0.25
Arctic Surface Warming/Cooling (ASW/C)	-	0.125/-0.125
$\frac{\partial T}{\partial t}\lvert_{ASW/C} = A_0 \cos^{15}(\phi - \pi/2) \exp[6(\frac{p}{p_0} - 1)], \quad (\phi > 0)$	-	0.25/-0.25
$F(p) = 0$	-	0.5/-0.5
	-	1.0/-1.0
	-	2.0/-2.0

Table 2.1: A list of the numerical values used in the thermal perturbation runs. For the TTW and TUW runs, the parameters in Eq. (2.1) are altered: $F(p)$ and $W(\phi, \phi_0)$ set the vertical and meridional structure of the heating, where ϕ_0 is the latitudinal width of the warming perturbation and $\delta\phi = 5°$ sets the meridional sharpness of the thermal perturbation boundary. For the ASW/C runs, an additional heating rate is specified by $\frac{\partial T}{\partial t}\lvert_{ASW/C}$ with $F(p) = 0$. For all the runs, A_0 is the magnitude of the heating, and p_0 is 1000hPa. Notice the ASW have positive A_0, and ASC have negative values. All the simulations are run at the R30 resolution, and the bold numbers in TTW indicate the simulations conducted at R60, T42, and T85 resolutions.

boidal 30 (R30) spectral harmonic truncation with 20 vertical levels is primarily used with eighth-order horizontal hyperdiffusion with a damping time scale of 0.1 day for the smallest resolved scales. The model is integrated for 12,000 days using the last 11,500 days after spin-up. The parameters for this study are presented in Table 2.1 and described in more detail below. Note the bold numbers in the ϕ_0 and A_0 columns indicate simulations that are run at the different resolutions and truncations.

More specifically, the radiative-equilibrium-temperature profile is given as

$$T_{eq} = \max\left\{200, \left[315 - \Delta T \sin^2\phi - \Delta T\ F(p)W(\phi,\phi_0) - \delta_z \log\left(\frac{p}{p_0}\right)\cos^2\phi\right]\left(\frac{p}{p_0}\right)^{\kappa}\right\} \tag{2.1}$$

where ϕ is latitude, p is pressure, $p_0 = 1000$ hPa, $\Delta T = 60$ K, and $\delta_z = 10$ K. $F(p)$ and $W(\phi,\phi_0)$ are functions, see below for more details, that set the vertical and horiztonal thermal structures, respectively. For the [44] control configuration, $F(p)$ is set to zero in Eq. (2.1). Four types of thermal perturbations are outlined below including altering ΔT as in [42], tropical tropospheric warming, tropical upper-tropospheric warming and Arctic surface warming/cooling [19, 88, 17]. The first perturbation is very simply an increase and decrease in the ΔT term in Eq. (2.1). ΔT values are 40 K, 50 K, 70 K, and 80 K, where 40 K represents a decrease in the equator-to-pole temperature difference and 80 K an increase. The next two perturbations are imposed by altering the parameters in the radiative-equilibrium-temperature, Eq. (2.1), and the third one is introduced by an additional heating rate, $\frac{\partial T}{\partial t}|_{AS\,W/C}$.

Jet latitudes and speeds are used extensively throughout this study. The 850 hPa time- and zonal-mean zonal wind is linearly interpolated to a resolution of $\sim .22^\circ$ to get a higher resolved representation of the jet statistics. For example, the R30 data has a meridional resolution of $\sim 2.5^\circ$. When calculating the jet latitudes at this resolution, many of the experiments would be grouped into the same jet latitude. By using the interpolated field, a more accurate representation of the jet latitude can be determined. Using the interpolated field, the jet speed is simply the maximum wind speed. The jet latitude is defined as the latitude at which the jet speed is calculated. This method for jet speeds and latitudes is consistent with a polynomial fit definition used in [33]. The vertical gray lines in the four panels of Figure 2.1 illustrate a jet latitude of about 43° for

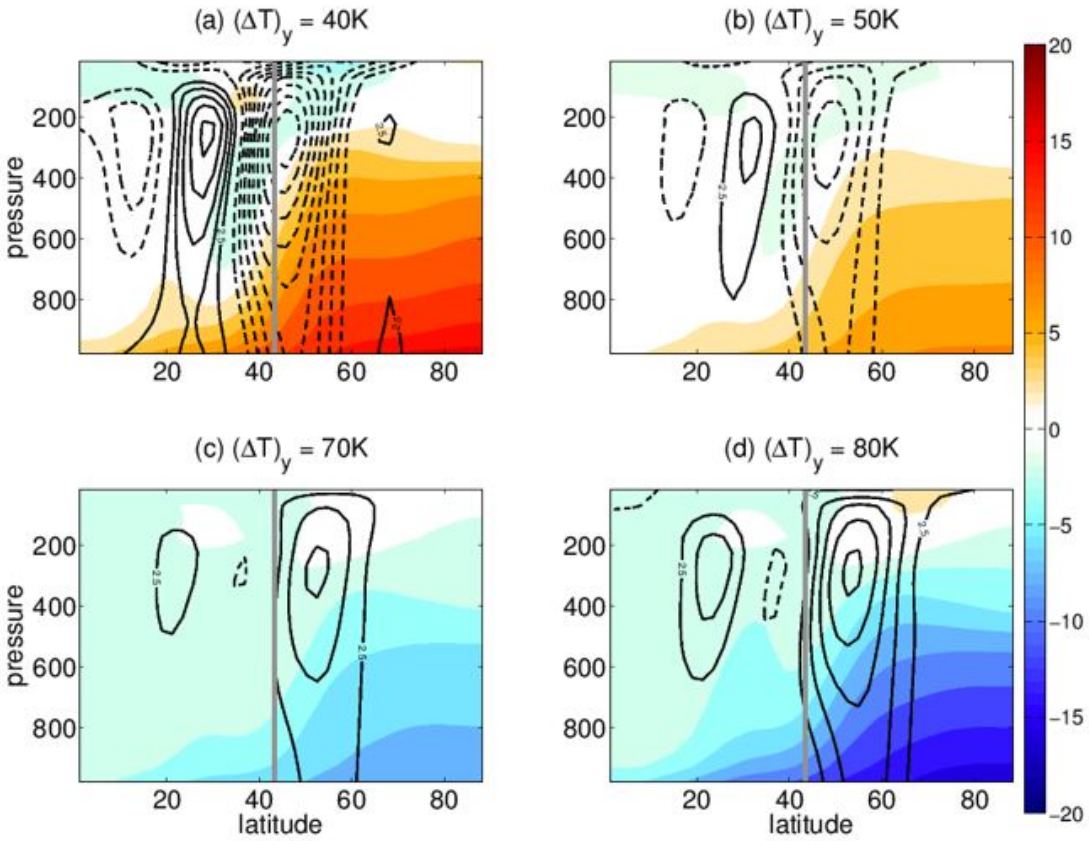

Figure 2.1: Responses in temperature (shades with a 2 K interval) and zonal-mean zonal wind in m s^{-1} (black contours) between ΔT runs and the control run for (a) ΔT = 40 K, (b) ΔT = 50 K, (c) ΔT = 70 K, and (d) ΔT = 80 K. Dashed contours are negative, and the vertical gray line in each plot indicates the climatological jet latitude for the control run.

the control simulation. The responses of the zonal wind and temperature from the control run are also shown in Fig. 2.1 for the ΔT runs. The response to increasing ΔT produces a cooling pattern in the Arctic regions and throughout the midlatitudes. The mean wind response is a poleward shifted jet latitude with a strengthening midlatitude jetstream and the development of a well separted subtropical jet. In contrast to this, an Arctic warming signature, i.e. by reduc-

ing ΔT, the midlatitude jet shifts equatorward, weakens, and merges with the subtropical jet. Concurrent with the equatorward shift and weakening of the jetstream with AA, there is a strong reduction in both the fluxes of eddy momentum and eddy heat (not shown). In all, AA produces a warming signature at high latitudes, equatorward and decelerated jetstream, merging of the eddy-driven and subtropical jet, and reduction in the eddy fluxes, consistent with [42]. The next subsections will describe the more realistic thermal perturbations used.

2.1.1 Tropical Tropospheric Warming (TTW)

The functions $F(p)$ and $W(\phi, \phi_0)$ in Eq. (2.1) are designed to increase the radiative-equilibrium-temperature of [44] in the tropical troposphere without altering the stratospheric temperature. As mentioned above, $F(p)$ defines the vertical structure of the thermal perturbation, and $W(\phi, \phi_0) = 0.5\{1 - \tanh[(|\phi| - \phi_0)/\delta\phi]\}$ is a weighting function that sets the meridional structure with ϕ_0 setting the boundary of the warming and $\delta\phi = 5^\circ$ setting the sharpness of the boundary. A narrow warming with $\phi_0 = 10^\circ$ and a broad warming with $\phi_0 = 30^\circ$ are used and described in Table 2.1.

To produce a warming signature that is independent of height in the tropical troposphere, $F(p)$ in Eq. (2.1) is set to a constant, A_0, and thus it produces a warming throughout the depth of the troposphere. This thermal structure does not alter the stratospheric temperature profile. Similar to Fig. 2.1, Fig. 2.2a,b plots the zonal wind and temperature response compared to the control run for both narrow ($\phi_0 = 10^\circ$) and broad ($\phi_0 = 30^\circ$) warmings compared

with the control run. These two examples have used the quadrupled parameter of $A_0 = -0.25$ with the radiative-equilibrium-temperature profile change indicated by green contours, see details of A_0 below. The prescribed radiative-equilibrium-temperature change produces local warming plus an indirect remote temperature change associated with the change in dynamics of the general circulaton, i.e. the tropical and midlatitude circulations. The response of the zonal wind, shown in black contours, is an equatorward shifted and strengthened jetstream, while the broad warming produces a poleward shift and similar strengthening, both in response to an increase the midlatitude temperature gradient and variability. [88] have shown that this opposite response in jet shifts for the TTW cases can be explained as a tug-of-war between the low-level baroclinity and an increase in subtropical wave breaking which can alter both the magnitude and latitude of the eddy momentum fluxes. There is also an increase in the zonal wind in the tropics and subtropics for the narrow and broad warming cases, respectively.

The magnitude of the heating is altered for both narrow and broad experiments, in order to produce experiments with a systematic shift in jet latitude. This is done by quartering, halving, doubling, and quadrupling the standard perturbation simulation (i.e., $A_0 = -0.0625$). Runs are performed with $A_0 = -0.015625$ for the quarter run, $A_0 = -0.03125$ for the half run, $A_0 = -0.125$ for the double run, and $A_0 = -0.25$ for the quadruple run. This produces ten experiments with jet latitudes ranging from about 40° to 50°. Although the eddy-driven jet does not reach latitudes as far poleward as the SH eddy-driven jet, i.e. about 52°, these model settings are used to obtain a variety of possible jet latitudes to analyze eddy-mean flow feedbacks and extreme event statistics.

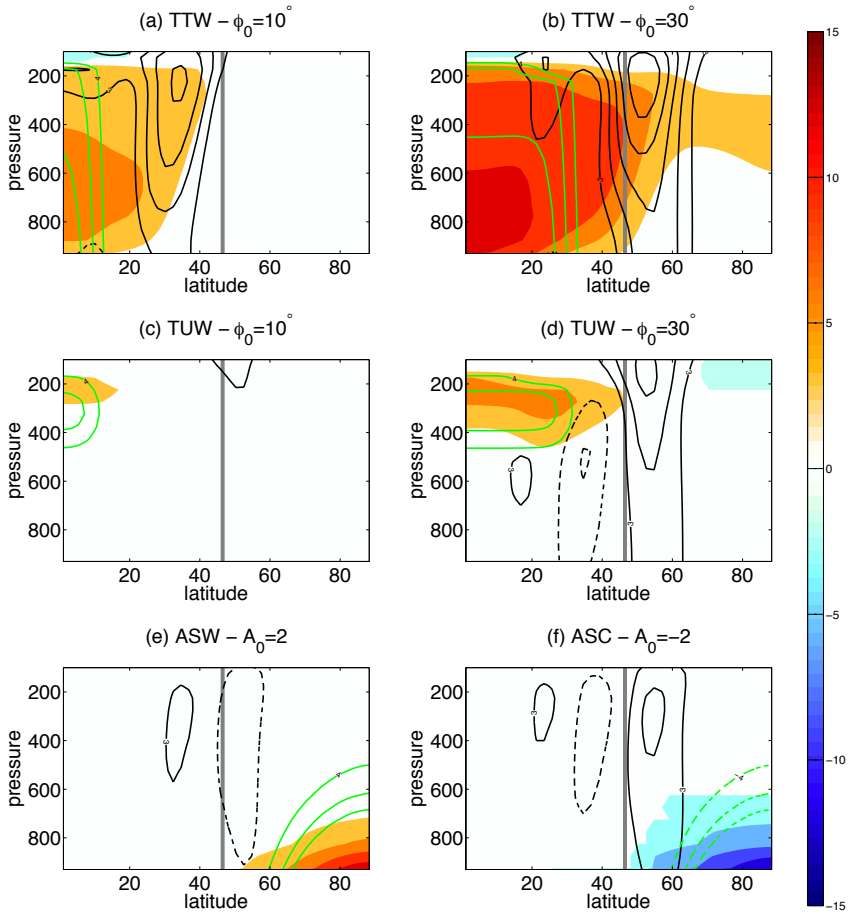

Figure 2.2: Same as Fig. 2.1 but also includes the response in the radiative-equilibrium-temperature profiles (green contours at 4 K, 8 K, and 12 K) for (a,b) tropical tropospheric warming (TTW) runs, (c,d) tropical upper-tropospheric warming (TUW) runs, and (e,f) Arctic surface warming and cooling (ASW/C) runs. For the TTW and TUW runs, 10° wide runs are in the left column, and 30° wide runs are in the right column. For the ASW/C runs, the left column is warming, and the right column is cooling. Each forced run uses the quadrupled value of A_0 which shows the biggest forced response.

2.1.2 Tropical Upper-tropospheric Warming (TUW)

In order to produce a tropical warming that depends on height, $F(p)$ is no longer set to a constant but is allowed to vary as $F(p) = A_0 \exp\left[-(p/p_0 - 0.3)^2/(2 \times 0.11^2)\right]$ in Eq. (2.1) to produce a tropical upper-tropospheric warming (TUW) signature [19, 88, 17]. The temperature and wind field responses are shown in Fig. 2.2c,d. In contrast to the TTW runs, the response of the climatological zonal wind is a poleward shift for both narrow and broad warming cases in comparison to the control run. The zonal wind shift is much smaller and weaker for the narrow warming. [88] have shown that the shift in zonal wind for a broad warming can be explained by an increase in effective diffusivity associated with enhanced irreversible potential vorticity mixing in the subtropics, consistent with poleward shifts in both cyclonic and anticyclonic wave breaking for the broad warming scenario [60] and poleward shifted eddy momentum forcing. As for the TTW runs, the magnitude of the heating is altered by quartering, halving, doubling, and quadrupling the standard perturbation runs for both narrow and broad experiments, and thus a range of changes in jet latitude are produced, see Table 2.1.

2.1.3 Arctic Surface Warming/Cooling (ASW/C)

An Arctic amplification-like signature is generated by using a thermal forcing from [19]. A thermal forcing is applied to the Northern Hemisphere by prescribing the additional heating rate as

$$\frac{\partial T}{\partial t}|_{ASW/C} = A_0 \cos^{15}(\phi - \pi/2) \exp[6(\frac{p}{p_0} - 1)], \quad (\phi > 0) \tag{2.2}$$

with p_0 = 1000 hPa. The equivalent change in T_{eq} can be inferred by multiplying the heating rate with the radiative relaxation time scale. The interpretation of a heating rate is that if the heating rate is equal to 1 day, the temperature profile would be exactly relaxed to the equilibrium temperature profile, erroding all general circulation features. Instead, the heating rate value is large, since it is one over the heating rate in the temperature tendency equation, and slowly relaxes the temperature profile over many time steps allowing the evolution of the general circulation. The temperature and wind field responses are shown in the bottom row of Fig. 2.2. As in [19], a low-level warming in the Arctic shifts the jet equatorward, and conversely, cooling in the Arctic shifts the jet poleward. Similar to the TTW and TUW runs, five magnitudes of Arctic surface warming (ASW) are applied, including A_0 = 0.125 for the quarter run, A_0 = 0.25 for the half run, A_0 = 0.5 for the standard run, A_0 = 1 for the double run, and A_0 = 2 for the quadruple run. Also, five Arctic surface cooling (ASC) runs are conducted by reversing the sign of A_0, which produces jet shifts in the opposite direction. This leads to ten ASW/C runs. In all of these simulations, ΔT, TTW, TUW, and ASW/C runs, the climatological jet system is characterized by a blurred subtropical and eddy-driven jet except for the farthest equatorward jets that merge the two jet systems together.

[88] have found that the responses of zonal wind to idealized thermal perturbations are qualitatively similar at higher resolutions, although the magnitude of the responses in zonal wind is smaller, as expected from the fluctuation-dissipation theorem [75, 37], due to the change in annular mode time scales with resolution. Given the qualitatively similar results at high resolutions, here we focus on the R30 simulations that can be used to explore a wide range in the model parameter space. Selected simulations are verified at R60, T42 and

T85 resolutions, see Table 2.1. A discussion will follow the main chapters and will describe sensitivities that the annular mode timescales and extreme event characterization have due to resolution and truncation.

In the interest of recreating this work or extending this work in the future, a brief description of the computational requirements is described. The model is ran using the National Center for Atmospheric Research's Yellowstone supercomputer. For the low resolution simulations (R30 and T42), the model is ran on a single node with sixteen tasks or processors per node. With this computational configuration, 6000 output days are processed in approximately three hours for seven output variables. For every 500 days of daily data, one variable is 0.25 gigabytes. For the higher resolved simulations (R60 and T85), the model is ran on two nodes with sixteen tasks per node. For 6000 days of daily data, it takes four hours to generate the output for seven output variables. For every 500 days of daily data, one variable is nearly one gigabyte. I would like to acknowledge high-performance computing support from Yellowstone (ark:/85065/d7wd3xhc) provided by NCAR's Computational and Information Systems Laboratory, sponsored by the National Science Foundation.

2.2 Finite-Amplitude Wave Activity

The finite-amplitude wave activity (FAWA) framework introduced by [69] is used but applied to the 500 hPa geopotential height (Z500) field as in [20]. The waviness of Z500 contours is defined as

$$A = \frac{1}{2\pi a \cos\phi_e}\left(\int\int_{Z500<\hat{Z},\phi\geq\phi_e(\hat{Z})} Z500 d\mathbf{S} - \int\int_{Z500\geq\hat{Z},\phi<\phi_e(\hat{Z})} Z500 d\mathbf{S}\right) \tag{2.3}$$

where A is the wave activity and $d\mathbf{S} = a^2 \cos\phi \mathrm{d}\lambda \mathrm{d}\phi$. The equivalent latitude, ϕ_e, corresponds to the Z500 contour, $Z500 = \hat{Z}$, such that the area enclosed by the $\hat{Z}$ contour toward the North Pole is equal to the area enclosed poleward of ϕ_e [18]. A physical interpretation of wave activity is to consider a Z500 field that is zonally symmetric and decreasing toward the pole. This would provide a wave activity of zero, whereas Z500 contours with excessive north-south undulations provide a positive definite quantity of wave amplitude. Larger wave amplitudes correspond to larger values of A. The motivation for applying the FAWA formalism to the Z500 field is that [20] have shown that the wave activity responds to the low-level baroclinicity which is intimately related to the eddy-driven jetstream, see Eq. (9) in [20]. Wave activity is used in Chapter 6 to link changes in wave amplitudes to changes in the number of extreme events.

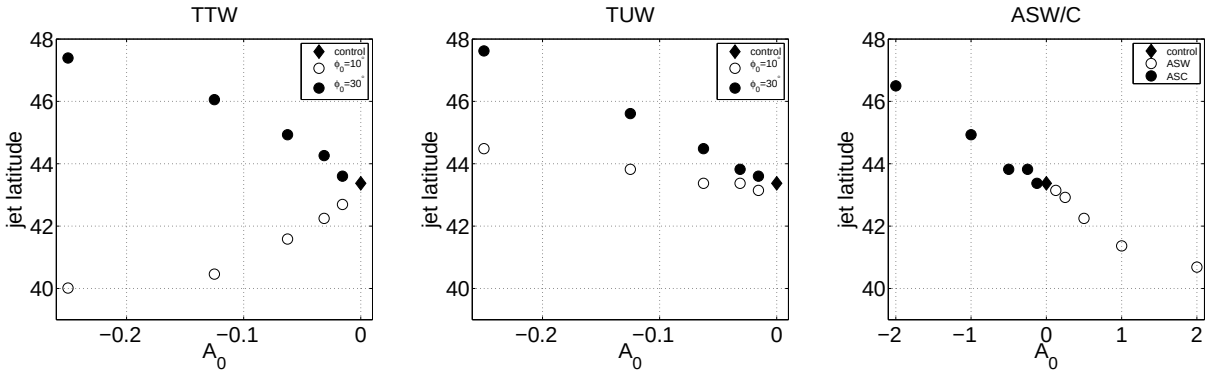

Figure 2.3: Climatological jet latitude as a function of forcing strength for (left) tropical temperature warming (TTW) runs, (middle) tropical upper-tropospheric warming (TUW) runs, and (right) Arctic surface warming/cooling (ASW/C) runs. Closed circles indicate broad warming runs (e.g. $\phi_0 = 30°$) for the TTW and TUW runs (left and center) and also for ASC runs (right) (e.g. negative values of A_0).

2.3 Summary

Figure 2.3 summarizes the direction of the jet shift with respect to the magnitude of the individual thermal forcings that have been elaborated in Section 2. Note the ΔT runs are not shown here but exhibit a linear increase in jet latitude with increasing ΔT. The jet latitude response in Fig. 2.3 is approximately linear to the magnitude of the forcing, yielding a range of jet latitudes. Again, these jets do not reach latitudes as far poleward as the SH eddy-driven jet, but the experiments were designed to provide a range of possible jet latitudes to analyze. The response to the TTW narrow warmings is an equatorward shift of the zonal jet and to broad warmings a poleward shift. Both narrow and broad warmings for the TUW runs shift the jets poleward. The ASW scenarios shift all the jets equatorward, while the ASC scenarios shift the jets poleward. As the mechanisms of the climatological jet responses to tropical warming have been examined in [88] and [60], the question now becomes, how does the climatological jet latitude affect the time scales associated with the annular mode?

CHAPTER 3

ANNULAR MODE TIME SCALES

As discussed in the Introduction, the jetstream varies in jet latitude in response to various observed and modeled forcings. No matter which latitude the midlatitude jetstream resides at, it is important to understand how the internal dynamics of the jet system will respond to changes in its latitude. This chapter will utilize principal component analysis and feedback analysis [84, 70] to determine changes in the time scales of the north-south meandering of the eddy-driven jetstream to idealized climate change scenarios. The chapter will have three main sections. The first section will use the control run to describe the methodology used to analyze jetstream time scales. A section will follow to determine the effect jet latitude has on persistent shifts in the midlatitude jetstream. Namely, if the climatological jetstream is located at a higher latitude (say due to greenhouse gas forcing), how will this affect the time scales of persistent jet shifts? The results are tested for model resolution and grid truncation to determine if sensitivities exist from this analysis. The chapter concludes with a brief summary.

3.1 Method

As is common in annular mode variability analyses, the principal component time series of the vertical- and zonal-mean zonal wind in the extratropics (between 20° to 70° latitude), weighted by $\sqrt{\cos\phi}$ following [3], is used to describe the north-south shifting of the midlatitude jetstream from climatology and is referred to as z, the zonal index. Before describing the dynamics of z (Eq. 3.3

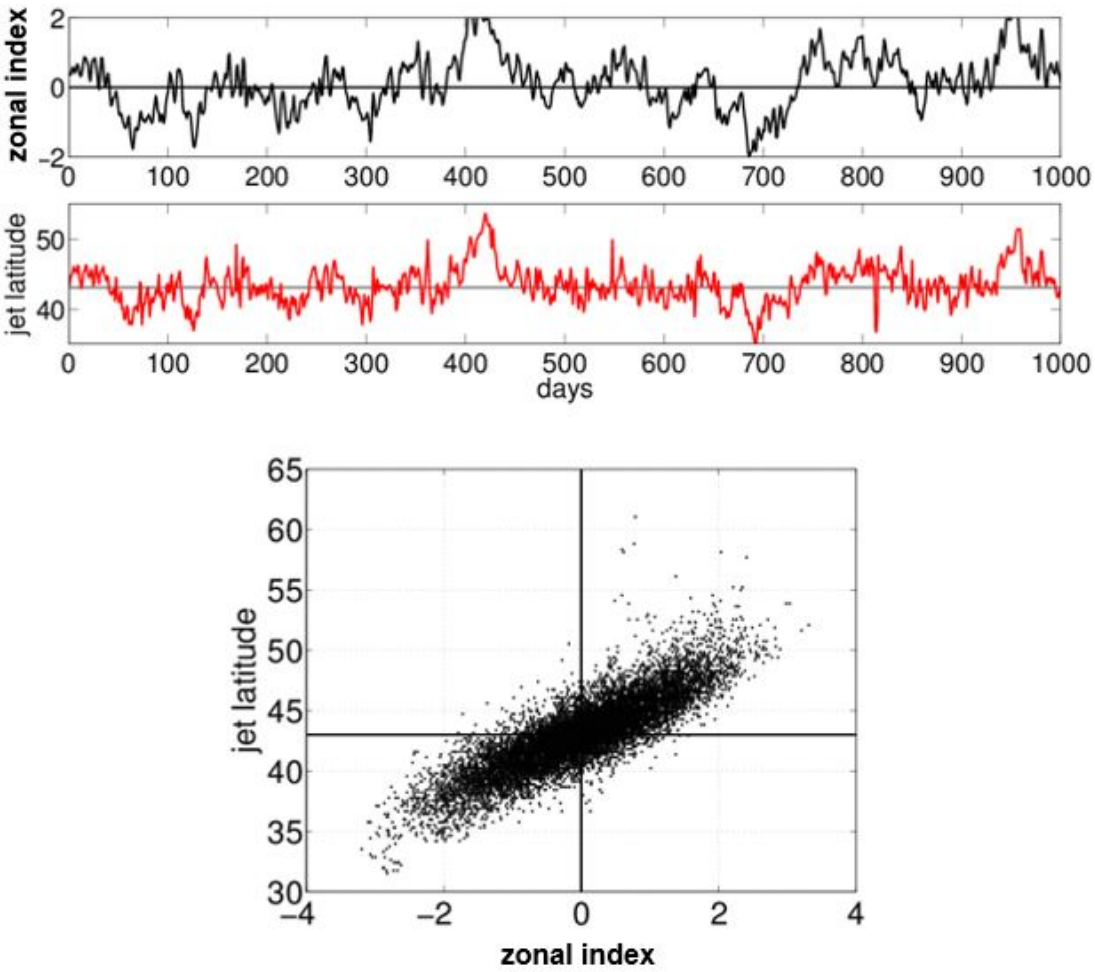

Figure 3.1: Top panel: the zonal index (leading principal component time series of the vertical- and zonal-mean zonal wind) as a function of model day. Middle panel: daily jet latitude (calculated as the latitude at which the climatological jetstream maximizes at the 850 hPa level) as a function of model day. Bottom panel: scatterplot of the daily values of the zonal index and the jet latitude.

below), Fig. 3.1 demonstrates what z describes. It is clear that there is a strong relationship between the eddy jet latitude and z, where positive z indicate a poleward shifted jet (in comparison to its climatology) and a negative z value for an equatorward shifted jet. This is further demonstrated in the bottom panel, which shows a scatterplot of the daily z and jet latitude values, showing a strong correlation between the two. For this reason, the z and jet latitude may be used interchangeably.

The associated empirical orthogonal function (**E**) structure, in ms^{-1}, is demonstrated in Fig. 3.2 as a regression onto the standardized z values. As in the SH observations [56], the poleward shift of the jet in the positive phase of the annular mode is associated with a similar poleward shift in the eddy momentum flux convergence (in panel (b)), an eddy momentum feedback at lag +10 days (not shown). The low-level baroclinic source also shifts poleward in association with the poleward jet shift, also an eddy feedback at lag +10 days (not shown). As reviewed in the Introduction, previous studies have attributed either the upper-level wave propagation and wave breaking or the lower-level baroclinic source to the poleward jet shift in the SH as well as the extended persistence of the anomalous zonal wind [56, 70]. The time scale of jet variability for the control run is also demonstrated in the right panel of Fig. 3.2. Observations show an intraseasonal variability of the e-folding time scales ranging from about 6 to 20 days in the troposphere for both the NH and SH [4]. With regard to the [44] system, [37] found the annular mode time scale converges to 20 to 25 days at sufficiently high horizontal and vertical resolutions. The autocorrelation of z is shown along with a horizontal line depicting the e-folding time scale. For the control run, a decorrelation time scale of 43 days (the number of positive lag days it takes for the z autocorrelation to fall below $1/e$ in Fig. 3.2c) suggests the

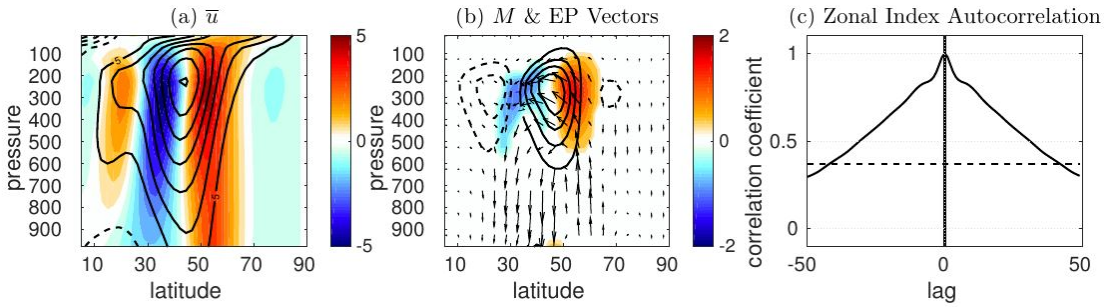

Figure 3.2: Control run climatology (contours) and lag 0 regressions onto the zonal index (shades), representing the leading mode of variability, for (a) zonal-mean zonal wind and (b) eddy momentum flux convergence and Eliassen-Palm vectors. Negative contours are dashed. The contour intervals for the regression in (a) are 0.5 m s^{-1} and (b) are 0.2 m (s day)$^{-1}$. Climatology contour intervals are indicated in the figure. (c) Lagged autocorrelation of the zonal index from Fig. 3.1. The horizontal dashed line is the value of the e-folding time scale.

model dynamics are far too persistent and may result from model resolution or a lack of zonal asymmetries in this model configuration [37].

This analysis will just analyze the eddy feedback as a whole and not its individual constituents, see [17] for this. It is well recognized that the vertical- and zonal-mean zonal wind is driven by eddy momentum flux convergence and damped by surface friction (e.g. [56]) and can be written as

$$\frac{\partial < \overline{u} >}{\partial t} =< M > - < \overline{F_r} > \tag{3.1}$$

where $M = -\frac{1}{a\cos^2\phi}(\overline{u'v'}\cos^2\phi)_\phi$ is the eddy momentum flux convergence on the sphere, and $\overline{F_r}$ is the frictional damping acting on the zonal wind, $\overline{u}$. The vertical average for a variable X is calculated as $< X >= (1/p_s)\int_{100hPa}^{1000hPa} Xdp$ where $< X >$ is the vertical average of X. Using the fact that the eddy momentum is mainly

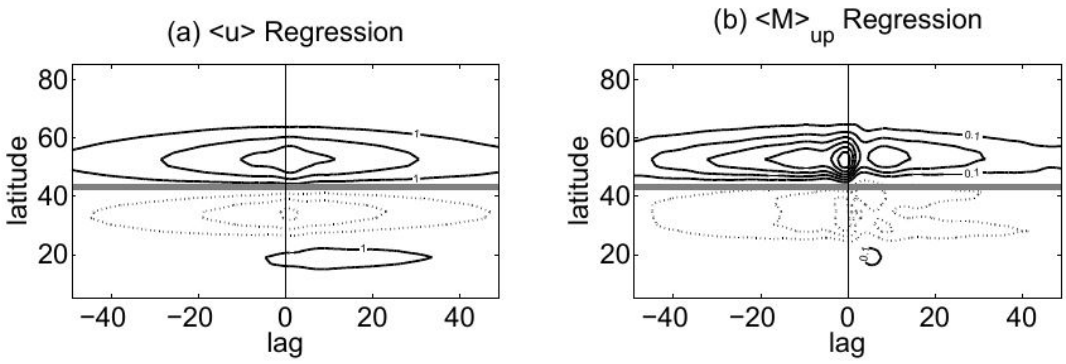

Figure 3.3: Control run lagged-regressions onto the zonal index for (a) zonal-mean zonal wind (m s^{-1}) vertically averaged from 1000 hPa to 100 hPa and (b) eddy momentum flux convergence (m s^{-1} day^{-1}) vertically averaged from 500 hPa to 100 hPa. Negative lags indicate eddy-time series lead the zonal index, while positive lags the zonal index leads. Negative contours are dotted. The horizontal gray line in each plot indicates the climatological jet latitude.

confined above 500 hPa, Eq. 3.1 can be simplified to

$$\frac{\partial < \overline{u} >}{\partial t} \approx < M >_{up} - < \overline{F_r} > \tag{3.2}$$

where the vertical average for $\overline{u}$ and $\overline{F_r}$ is calculated from 100 hPa to the surface and M is averaged from 100 hPa to 500 hPa. The vertical average for M is calculated as $< M >_{up} = (1/p_s) \int_{100hPa}^{500hPa} M dp$.

Before moving on to the annular mode time scale analysis, a brief description of the eddy feedback will be given. To better understand the temporal evolution of eddy momentum forcing associated with the annular mode variability, lagged-regressions of $< \overline{u} >$ and $< M >_{up}$ onto z are performed. Figure 3.3 demonstrates a lagged-regression of $\overline{u}$ (left panel) and $< M >_{up}$ (right panel) onto the zonal index time series. The zonal wind is highly persistent, with lifetimes beyond ± 50 days, in agreement with the decorrelation time scale presented

above. The right panel shows that the zonal wind shift is initially eddy driven because the zonal wind shift occurs after the eddies (indicated by a negative lag in Fig. 3.3) and subsequently eddy prolonged (positive lags). This eddy feedback extends the persistence of an eddy-driven jetstream and shows that the annular modes are very useful for weather predictability, e.g. if a shift in the jetstream is predicted, there can be some confidence suggesting it may persist in this location for upwards of 40 days in this control simulation.

Although each component in the eddy feedback mechanism, such as barotropic mixing, baroclinic pumping, and wave transience, is not analyzed, the feedback associated with the total eddy momentum feedback is described to understand changes in the jetstream time scales. A compact analysis of eddy feedback mechanisms, as in [84] and [70], can be demonstrated by first computing the eddy time series through projecting $< \overline{X} >$ onto the leading **E** as $x(t) = < \overline{X} >$ **WE**/**EWE**, where x indicates the portion of $< \overline{X} >$ that projects onto **E**, and **W** is the diagonal weighting matrix of $\cos\phi$ [3]. It follows that the zonal-mean zonal wind tendency equation (Eq. (3.2)) can be projected onto the annular mode as [70]

$$\frac{\partial z}{\partial t} = m_{up} - \frac{z}{D} \tag{3.3}$$

where m_{up} is a time series that denotes upper-level eddy momentum flux convergence. D denotes the time scale of frictional damping acting on the annular mode. Equation 3.3 is a zonal index tendency equation that describes the north-south fluctuation of the eddy jetstream demonstrated in Fig. 3.1. A positive m_{up}, momentum convergence, corresponds to a poleward shift in jet latitude and a negative m_{up}, momentum divergence, to an equatorward shift.

A lagged-covariance structure between the eddy forcing time series in Eq.

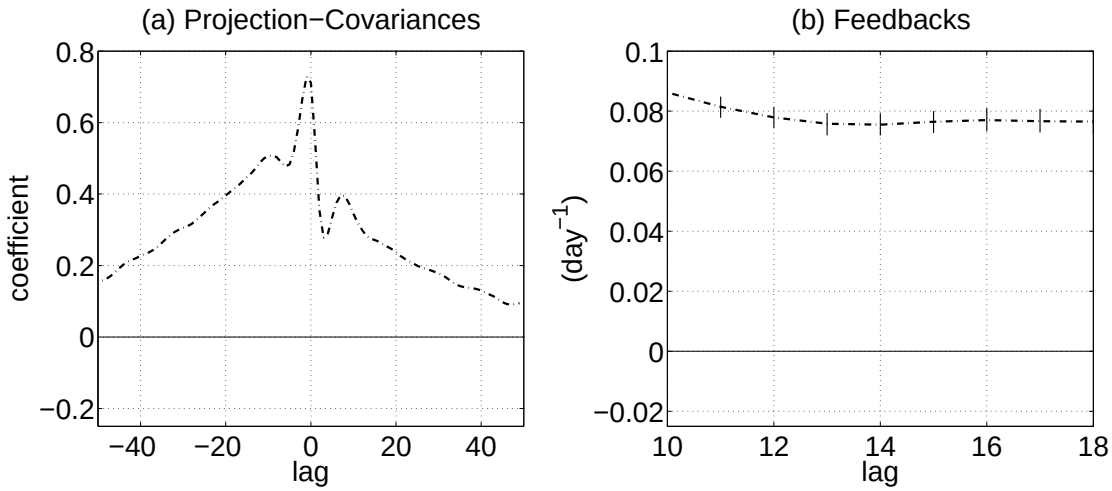

Figure 3.4: Control run eddy momentum flux convergence of (a) the lagged covariance of eddy time series in Eq. (3.3) onto the zonal index (units: (m s^{-1})^2 day^{-1}) and (b) feedback strength. Vertical lines in (b) indicate the 95% confidence intervals based on 1,000 bootstraps (see text for calculation details.)

(3.3) and z is displayed in Fig. 3.4a, where a positive value indicates an eddy forcing that supports a poleward jet, and positive lags indicate z leads the eddy forcing time series, a feedback. As for the observed annular mode [56], the eddy momentum flux convergence contributes positive values in both negative and positive lags that separately drive the jet poleward and sustain the jet at a poleward position, similar to Fig. 3.3. A secondary peak in eddy momentum is observed near lag +10 days and indicates that the eddies are sustaining the zonal wind against frictional damping to extend its persistence. This feedback increase has received much attention in the literature dating back to [56, 57].

In comparison with the lagged-covariance between the eddy forcing and z in the observed southern annular mode variability (cf. Fig. 2 of [70]), these results are qualitatively similar yet exhibit some quantitative differences. First,

as mentioned above, the time scale is overly long, indicating too much persistence, as a result of the idealized model physics and coarse model resolution. This leads to an overall momentum forcing strength that is excessively strong and supports the highly persistent poleward wind shift. This is not evident in the observations.

Finally, a recently developed technique designed to quantify eddy feedback to jetstream persistence ([84, 70]) is used. [56] suggests that the forcing of z can be separated into two components such that m_{up} in Eq. (3.3) can be parameterized as the random component $\tilde{m}_{up}$ that initiates a zonal wind shift plus the linearly dependent, eddy feedback part $b_{up}z$, where b_{up} represents the feedback strength. Decomposing the eddy momentum forcing time series, m_{up}, into its components gives

$$m_{up} = \tilde{m}_{up} + b_{up}z. \tag{3.4}$$

[84] have shown that the individual contributions from synoptic-scale and planetary-scale waves to eddy feedback can be estimated through lagged-regression analysis. Regressing the time series of m_{up} and z onto z with a lag of Δt implies that $m_{up}(t + \Delta t) \approx \beta_m^{\Delta t} z(t)$ and $z(t + \Delta t) \approx \beta_z^{\Delta t} z(t)$, where $\beta_m^{\Delta t}$ and $\beta_z^{\Delta t}$ are the regression coefficients of m_{up} and z at lag Δt, respectively. At large lags, the random component of the eddy forcing, $\tilde{m}_{up}$, should be nearly zero since the eddy forcing is mainly driven by the zonal flow at these lags. Substituting these values into Eq. 3.4 and solving for the feedback strength implies that the feedback strength can be computed as $b_{up}^{\Delta t} = \beta_m^{\Delta t} / \beta_z^{\Delta t}$.

Figure 3.4b gives these feedback strengths as a function of lag. The relatively constant feedback strength indicates the validity of this linear model. A positive feedback indicates a supporting role in maintaining a jet shift, while a negative

feedback indicates a dampening of z. Also provided in the plot are the 95% confidence intervals associated with the bootstrap method described in [84]. The method randomly samples the daily data with replacement to compute confidence intervals of the feedback strength. For each lag day, 1000 bootstraps are performed to provide a large sample of possible feedback values. The two-tailed, confidence intervals are then determined for the 1000 random samples, indicated by vertical lines for each process and lag. Looking at positive lags when the zonal wind anomaly reinforces the eddies, the black line indicates a positive feedback that sustains a poleward shifted jetstream, consistent with Fig. 3.3. Overall, there is good agreement between the modeled variability and the observed annular mode variability [70]. The following section will use these z and eddy feedback calculations to determine the response of annular mode time scales to changes in jet latitude.

3.2 Results

Having demonstrated the eddy forcing covariances in Fig. 3.4a, the feedback calculation in Fig. 3.4b, and the calculation of τ, the decorrelation time scale of the zonal index, this section will report the same analysis on all the idealized thermal perturbations including the tropical tropospheric warming (TTW), tropical-upper tropospheric warming (TUW), and Arctic surface warming/cooling (ASW/C). Starting with the low resolution (R30) model output, the zonal index autocorrelations in Fig. 3.5a for the 30 thermally perturbed runs and the control run indicate a range of decorrelation time scales (e.g. when the autocorrelation falls below the e-folding threshold) from about 20 to 100 days. These values are plotted against climatological jet latitude in Fig. 3.5b and in-

dicate a strong trend with jet latitude, consistent with other modeling efforts [37, 6, 33]. In this idealized configuration, jetstreams located near 40° may persist for nearly 60 days in a poleward location. Whereas, a jetstream located near 50° may only take 20 days to recover to its climatological jet latitude.

This demonstrates that with climate change, it is expected that the midlatitude jetstreams in both hemispheres will shift poleward in a warming climate. If this is the case, midlatitude weather predictability could be limited as the decorrelation time scales are so much lower. But on the other hand, ozone depletion has the opposite effect, and it is shown in the SH observations that a reduction in stratospheric ozone has led to a poleward shift in the jet latitude. Modeling efforts have shown that as ozone recovery continues, the eddy jet will tend toward an equatorward shift [86]. The limits of predictability may be enhanced in this case. AA also has the effect of shifting the jetstream equatorward, hence increasing the limits of predictability. Again, it will be the tug-of-war between these climate drivers that ultimately determines the midlatitude jet latitude, decorrelation time scales, and predictability limits.

The zonal index persistence feature can be noted in Fig. 3.5c which plots the lagged-covariance of m_{up} in Eq. (3.3) with respect to z for large positive lags where eddy feedbacks are expected. Consistent with the τ calculations, there is a general tendency to reduce the eddy forcing strength on the annular mode with an increase in jet latitude, where a poleward jet is reinforced by a much weaker eddy forcing compared with an equatorward jet. The total feedback strength associated with the eddy momentum flux convergence, $b_{up} = \beta_m^{\Delta t}/\beta_z^{\Delta t}$, in Fig. 3.5d exhibits this same feature. The more equatorward the jet latitude, the stronger the eddy feedbacks are. For the majority of the experiments these feedback val-

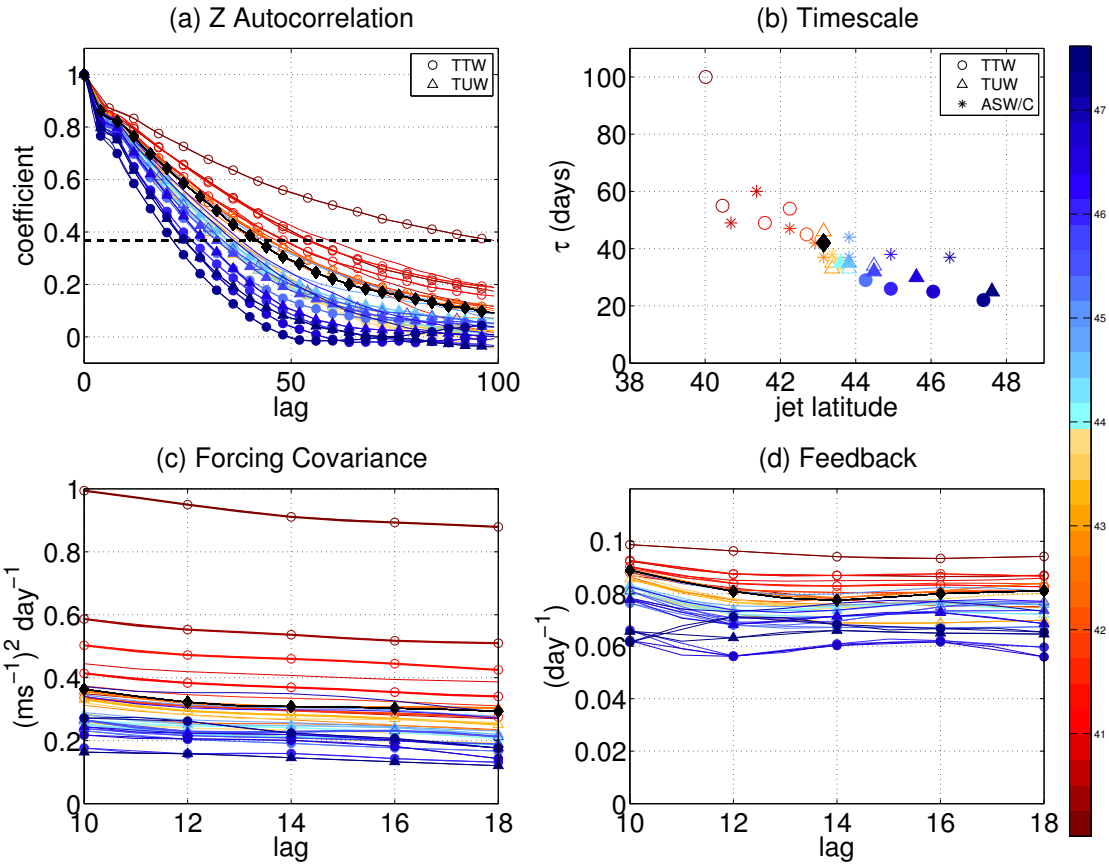

Figure 3.5: R30 truncation: (a) Zonal index lagged-autocorrelation (only positive lags shown). The horizontal black dashed line indicates the *e*-folding time scale. (b) *e*-folding time scale as a function of climatological jet latitude. (c) Lagged-covariance of m_{up} in (3.3) with the zonal index for positive lags when zonal index leads m_{up}. (d) Eddy momentum flux convergence feedback strength, b_{up}, as a function of positive lag. The colorbar, marker colors, and line colors for all plots indicate the latitude of the jet with warmer (red) colors for equatorward jet latitudes and cooler (blue) colors for poleward jet latitudes. Black lines and shapes represent the control run. Shapes for (a,c,d) are indicated in (a), and shapes for (b) are indicated in (b) with non-filled shapes representing narrow warming runs and filled shapes representing broad warming runs.

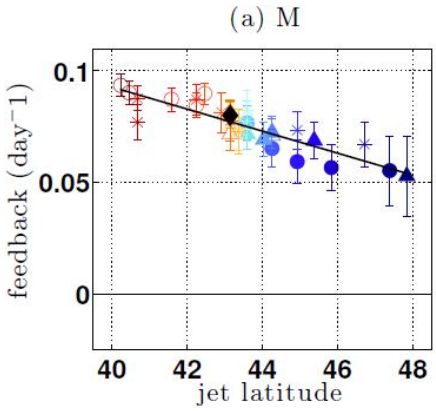

Figure 3.6: Eddy momentum feedback streghth, b_{up}, averaged over lags +10 to +18 days as a function of jet latitude. Colors are the same as Fig. 3.5. Black line is a linear best fit line. Error bars are computed from 1000 iterations using the bootstrap method; see text for more details.

ues are nearly constant over this lag period and give confidence that this linear model is sufficient to quantify eddy feedback strengths. The most poleward jet latitudes may suffer slightly from nonlinearities due to the rapid decorrelation time scales. Taking the average of these feedback strengths from lag +10 to +18 days and plotting them as a function of jet latitude in Fig. 3.6 further demonstrates the dependence between increasing jet latitude and decreasing annular mode decay time scales. Collectively, these results corroborate the reduction in feedback strength with an increase in jet latitude found in the phase 3 of CMIP models [5], and that the relationship is controlled by the large-scale eddy-mean flow interactions in the atmosphere.

Figure 3.7 summarizes the same diagnostics as Fig. 3.5, except for varied horizontal resolutions, each resolution consisting of five simulations. The zonal index autocorrelations indicate a range of decorrelation time scales ranging from about 15 to over 100 days. The higher resolution runs with poleward jet lati-

tudes allowed for the time scales to converge to that in the observations [4]. The z autocorrelations show a general trend for bluer (more poleward) jets to have shorter decorrelation time scales. These values are plotted against jet latitude in Fig. 3.7b and are now colored by their respective resolution and truncation. By focusing on one truncation and one resolution at a time, it is clear that each configuration demonstrates a reduction in annular mode time scales with higher jet latitude. There is also sensitivity where the poorly resolved, equatorward shifted jets exhibits time scales that are nearly an order of magnitude too large compared with higher resolved runs. But in general, each truncation and resolution configuration shows a reduction in the annular mode time scales with an increase in jet latitude. This is also corroborated by enhanced eddy forcing in panel (c), as evident in the lagged-covariance between the eddy momentum forcing and z, and the strength of the feedback parameter at different positive lags in panel (d).

3.3 Summary

The response of the annular mode decorrelation time scale to idealized climate change-like thermal perturbations is analyzed using a highly idealized, dry dynamical model from the Geophysical Fluid Dynamics Laboratory. By using different thermal perturbations, such as a tropical tropospheric warming, a tropical-upper tropospheric warming, and an Arctic surface warming/cooling, a wide range of jet latitudes are created. This allows for the analysis of the response of the decorrelation time scales to jet latitude, and it is corroborated that these idealized model configurations can model the midlatitude jetstream variability well, i.e. jet latitude, speed, annular mode time scales [56, 57], and

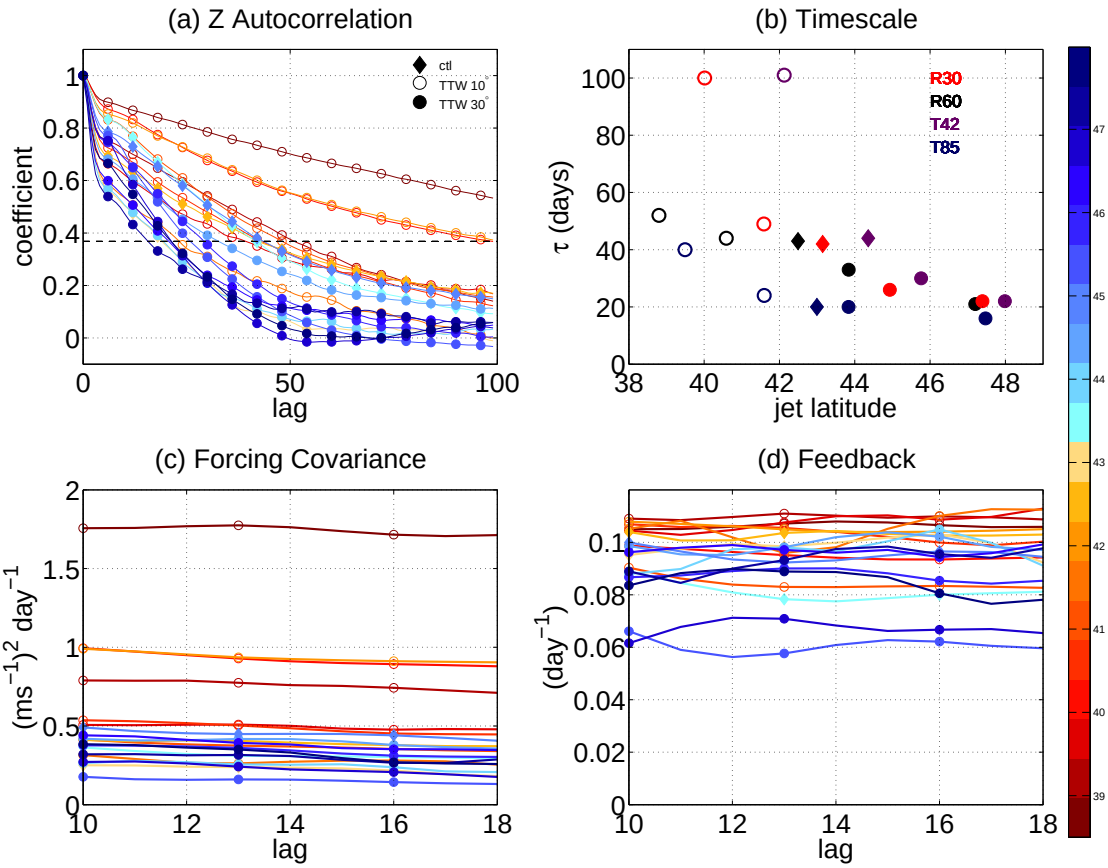

Figure 3.7: As in Fig. 3.5, except that the diagnostic is applied to different horizontal resolutions and truncations. In all the plots, open circles indicate the narrow tropical tropospheric warming (TTW) runs, closed circles indicate the broad TTW runs, and diamonds indicate the control runs for each resolution including R30, R60, T42, and T85. Experiments with the standard heating and quadruple heating are used (see bold numbers in Table 2.1). In (b), data points are not color coded by jet latitude, as in (a), (c), and (d), but are color coded by their resolution and truncation as indicated by the legend.

produce a decrease in time scales with an increase in jet latitude. Consistent with the reduction in time scales is a reduction in the eddy momentum feedback strength as the jet latitude increases leading to less persistent jet shifts. These results are tested for sensitivity to model truncation and resolution, and although sensitivities to which resolution is used (R30, R60, T42, and T85) exist, the general trend of a decrease in decorrelation time scales with an increase in jet latitude is robust. This reduction in time scales is again consistent with a reduction in the eddy momentum feedback strength.

CHAPTER 4

EXTREMES

A major question driving atmospheric research is whether the recent increase in certain types of midlatitude extreme weather events can be attributed to global climate change [23, 72]. Particular attention is currently being given to the effect that Arctic amplification (AA) will have on midlatitude dynamics. There is strong evidence that a major component of global climate change will be an AA signature whereby the high latitudes warm faster than the rest of the Northern hemisphere [81]. The effect of the unequal warming of the Northern hemisphere would be to reduce the equator-to-pole temperature difference, ΔT, thus leading to a reduction in the midlatitude meridional temperature gradient. It is proposed in [30, 53] that this reduction in ΔT would lead to a less meridionally confined jetstream. It is argued that by reducing ΔT, the jetstream would not be locked into a tight gradient and would be able to meander farther meridionally leading to a slower jetstream, amplified wave patterns, and more extreme weather. These types of slow moving, persistent weather patterns (e.g. blocking anticyclones) have been shown to concur with extreme weather events including cold air outbreaks e.g. [16] and heat waves e.g. [14, 27].

The AA hypothesis and its relationship to more extreme weather was directly tested in an idealized model configuration. By using a blocking definition based on a normalized 500 hPa geopotential (Z500) anomaly, it is determined that by reducing ΔT, a reduction in wave amplitudes and a robust reduction in persistent anomalies (i.e. anticyclonic blocks) occurs, an opposite response to that proposed in [30, 53]. Similar results are found in [32] who uses an idealized model configuration that allows the latitude of the jetstream to shift without

affecting the speed of the jetstream. Through an extreme event analysis, it is shown that with a reduction in the latitude of the jetstream (similar to the effect AA would have on the observed midlatitude jet), there is a robust reduction in the number of extreme events, again in opposition to [30, 53]. However, using multiple reanalyses datasets and multiple blocking algorithms, [7, 11] could find no clear hemispheric increase or decrease in wave amplitudes or blocking over the past 30 years (the time period of rapid sea-ice loss). [98] also analyzed four Coupled Model Intercomparison Project Phase 5 (CMIP5) models that exhibited the best blocking climatologies in the Atlantic sector and found no clear evidence suggesting a link between Arctic sea-ice loss, AA, and blocking over Greenland and Europe. Even if a trend can be detected in changes in persistent events, the internal variability of the climate system and the short observational record may mask changes in these events, as suggested in [82, 79]. With the complexities of the coupled climate system, multiple hypotheses for the change in persistent events, and the relationship between persistent and extreme events, a hierarchical approach can simplify the analysis.

This study extends the results in [42, 32] and analyzes both the effect jet latitude has on extreme events and the effect that jet speed has on extreme events. The following section discusses how to define an extreme event following the methodology of [32]. The second section is dedicated to the results using the R60 truncated data. The experiments being used in this section are the temperature difference, ΔT, runs and the tropical-temperature warming runs. A final section summarizes the results and describes sensitivies to resolution that are not found in the annular mode analysis.

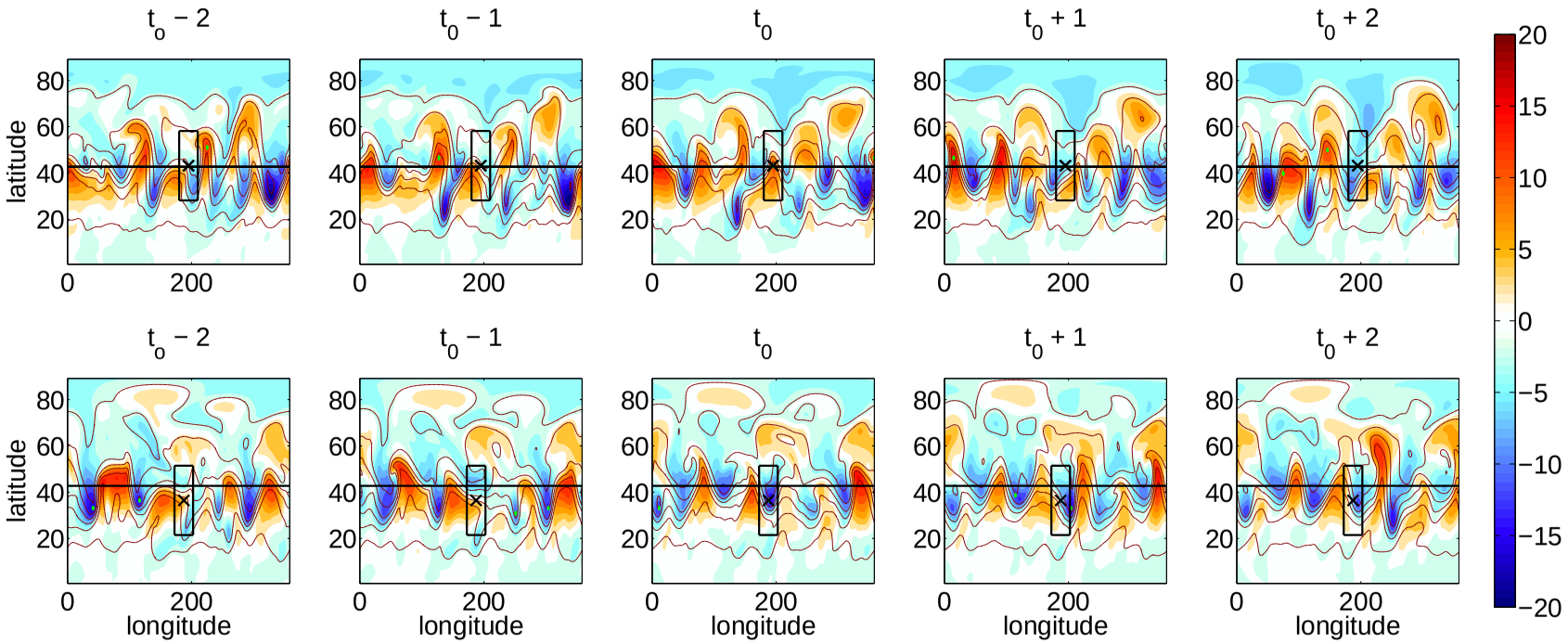

Figure 4.1: An illustration of the extreme event definition presented in [32] for a positive extreme event (top row) and negative extreme event (bottom row). An event is defined to occur on day t_0 in the middle column and day $t_0 - 2$ to $t_0 + 2$ are also shown across each row. Within each panel, the shades are the time-mean T850 anomalies (2 K contour interval), black horizontal contour is the climatological jet latitude, black box represents the 30° latitude-by-longitude box used to define an extreme event (see text for details). The subtle green dots throughout the domain show where other extreme events are occuring.

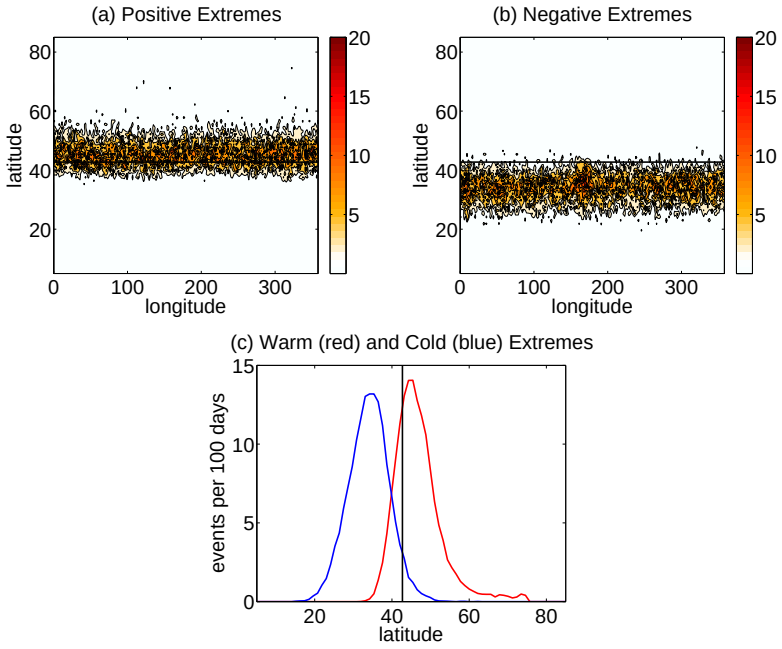

Figure 4.2: R60 control run mean extreme event statistics. Top row is the average number of events occuring at a particular grid point over a 100 day period for warm (left) and cold (right) extreme events. The contour interval and units for the top row are 2 events per 100 days. The bottom row shows the zonal average of the top panels for warm (red) and cold (blue) extremes. The climatological jet latitude is also plotted in all panels as a black contour.

4.1 Method

This section describes the procedure from [32] on how to compute an extreme event. The anomalies from the time-mean of the 850 hPa temperature field (T850, hereafter) are computed. The anomalies are then sorted from highest to lowest for every grid point in the domain. A threshold is then determined as the top and bottom 1% of the anomalies. The top 1% would correspond with positive temperature anomalies and the bottom 1% for negative temperature anomalies. For the R60 control run, the values of the 1% threshold are 11.0

K for the warm anomalies and -10.6 K for the cold anomalies. Two logical matrices are created from the three-dimensional (time, latitude, and longitude) anomaly matrix, one for each point exceeding the top 1% and one for each point falling below the bottom 1%. Each of these logical matrices are analyzed separately starting from the largest anomaly and ending with the anomaly that just exceeds the given threshold. Two criteria must be met in order for an anomaly to be considered an extreme event. The event must be spatially and temporally isolated. An anomaly must be spatially isolated in latitude and longitude by 30°. For a given anomaly that occurs on day t_0, the algorithm then checks from $t_0 - 2$ to $t_0 + 2$ to determine if the event is temporally isolated. This eliminates the issues of serial correlation by removing duplicate events that are long lasting in time. Unlike many blocking algorithms that have a strict persistence criterion, this extreme event algorithm is an isolation algorithm. If there is more than one event occurring within this spatial and temporal criterion, only the largest magnitude anomaly is kept.

Figure 4.1 illustrates both a positive anomaly extreme event (top panel) and a negative anomaly extreme event (bottom panel) from day $t_0 - 2$ to $t_0 + 2$. Starting with a positive extreme event, day t_0 (middle column) shows an event occurring near 200° longitude and 40° latitude. The event is occurring near or just poleward of the climatological jet latitude. As waves grow along the eddy jet latitude, poleward fluxing air crosses the jet latitude and brings with it warm subtropical air. This air enters a region of climatologically cooler air and becomes a large anomaly. The same feature can be noted for a cold event where cold equatorward fluxing air enters a region of climatologically warmer temperatures and becomes a large cold anomaly. This is why the structure of the anomalies is warm extremes on the poleward flank of the jet latitude and cold

extremes on the equatorward flank of the jet latitude, shown below. Starting on day $t_0 - 2$ in Fig. 4.1 for the warm extremes, the event is associated with a hemispherically amplified wave pattern and the actual event is a growing warm-air pool that penetrates to the poleward flank of the jet latitude. This algorithm is sensitive to the size of the 30° box. Clearly, the larger the search box is the fewer extreme events there will be. The algorithm has been tested using a standardized anomaly definition and using different percentile thresholds.

This is the first place where we see that a blocking algorithm is different from this extreme event algorithm. In a longitude-by-longitude blocking algorithm such as early definitions from e.g. [26, 95] and newer definitions from e.g. [42], the event in the top row of Fig. 4.1 would not be considered a persistent anomaly event. The anomaly propogates through the longitude very rapidly and would not persist long enough to be defined as a longitudinally isolated block. More recently, blocking algorithms have been developed to track either large wave breaking events (such as [12, 65]) or anomalies (such as [78, 24]). A tracking algorithm allows blocking statistics to be broken down into actual events that contain both requirements for a blocking event, i.e. large-scale and quasi-persistent. For the extreme event considered here (top row of Fig. 4.1), it is difficult to determine which type of blocking algorithm would identify this particular grid point as a persistent anomaly. This is, in essense, the strength of this extreme event definition from [32] which will only remove an event if it is not spatially or temporally isolated. A blocking algorithm, however, can remove events for many different reasons. A weakness of the extreme event definition, defined in the text above, is that it does not have any predictive power to understand persistent wave events, such as the annular modes or blocking events. Nevertheless, the extreme event diagnostic will be applied to the R60 runs to

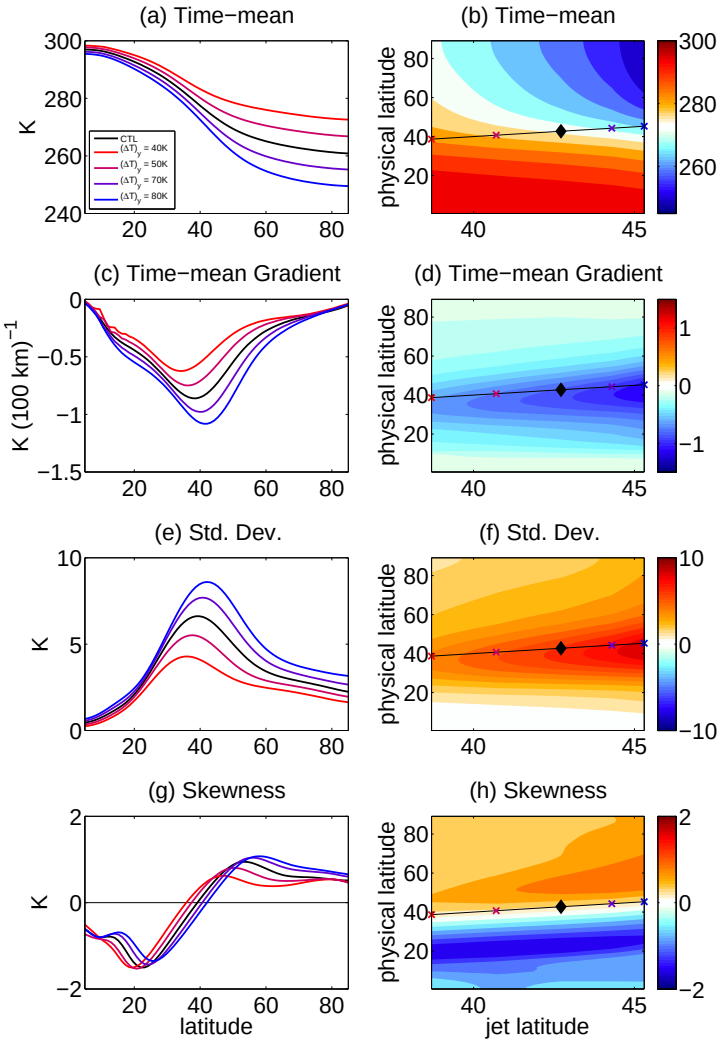

Figure 4.3: 850 hPa temperature (T850) statistics (described below) as line plots in the left column and a shaded plot in the right column. For the right column, each experiment's statistic as a function of latitude is placed at its jet latitude along the x-axis with physical latitude as the y-axis and extrapolated to form a contour plot. The colors of the lines in the left column and x's in the right column indicate the experiment with red for ΔT = 40 K and blue for ΔT = 80 K. Black lines and diamonds represent the control run (ΔT = 60 K). The first row, (a) and (b) is the time- and zonal-mean T850 in K; the second row, (c) and (d), is the meridional gradient of the first row (T850) in K(100 km)$^{-1}$; the third row, (e) and (f), is zonal-mean standard deviation of T850; and the fourth row, (g) and (h), is the zonal-mean skewness of T850 in K. The thin black lines in the right column indicate the one-to-one line for physical latitude and jet latitude. The contour intervals for (b) are 5.5 K, (d) 0.3 K(100 km)$^{-1}$, (f) 2 K and (h) 0.4 K.

determine the response in events to changes in jet latitude and speed.

Figure 4.2 demonstrates the mean extreme event statistics for the R60 control run. The time-mean, latitude-by-longitude cross section of the warm (left) and cold (right) extreme events shows a clear geographic dependence between the jet latitude and extremes. As mentioned above, the warm extremes are predominately situated on the poleward flank of the jetstream and cold extremes on the equatorward flank of the jetstream. Taking the zonal average of this plot in the bottom row of Figure 4.2 makes it clear how the jet latitude geographically marks the transition from cold to warm extremes. Each type of extreme has about 10 to 12 events occurring over a 100 day period (a seasonal time scale). The remainder of the experiments will be analyzed in the next section.

4.2 Results

This section will discuss the mean state response of the temperature difference, ΔT, runs followed by a discussion of the response of extreme events to other idealized thermal perturbations. Since the extreme event analysis utilizes the T850 field, a description of the T850 statistics will be given in Fig. 4.3. Each of the experiments is presented as a line plot in the left column. The right column then takes those five contour lines as a function of latitude and stacks them in a latitude band at their jet latitudes. This matrix is then plotted as a function of physical latitude space and jet latitude space. In panel (a), by reducing ΔT between the equator and pole, the temperatures are increased throughout much of the hemisphere with the most heating occurring in the polar regions. This has the effect of shifting the jet latitude equatorward, reducing the T850 meridional

gradient, and weakening the zonal wind speed, shown below. Concurrent with the reduction in T850 gradient and zonal wind speed is a weakening and equatorward shifting of the eddy heat and momentum fluxes (not shown). Panel (d) shows that the T850 gradient maximizes on the equatorward flank of the jet and supports a jetstream about 5° poleward of the maximum. In the regions of greatest T850 gradient, the variability of the field is also maximized where an AA signature (scanning from the blue line to the red line in the third row) leads to a reduction in the standard deviation. The variability is also maximized on the equatoward flank of the eddy driven jetstream.

Lastly, the fourth row plots the zonal-mean skewness. For T850, a positive skewness would indicate a long positive tail in the T850 distribution (more warm anomalies) and a negative skewness a long negative tail (more cold anomalies). As has been demonstrated before, T850 tends to be positively skewed on the poleward flank of the jet and negatively skewed on the equatorward flank. This feature is consistent with the bottom panel of Fig. 4.1 which shows that the warm extremes occur predominately on the poleward flank of the jet in regions with positive T850 skewness. The opposite is also demonstrated where in regions of cold extremes, the T850 is negatively skewed indicating cold temperature extremes. Now, in terms of an AA signature, the T850 response is to reduce the skewness on the poleward flank of the jet indicating a reduction in warm extreme events with AA, opposite to proposals from [30] and in agreement with results from [42, 32]. While the positive skewness tends to decrease on the poleward flank of the climatological jets as the jets shift equatorward, the negative skewness on the equatorward flank do not show the same trend. This may be an artifact of the jet latitudes that are being sampled, i.e. not enough poleward jets to see the trend.

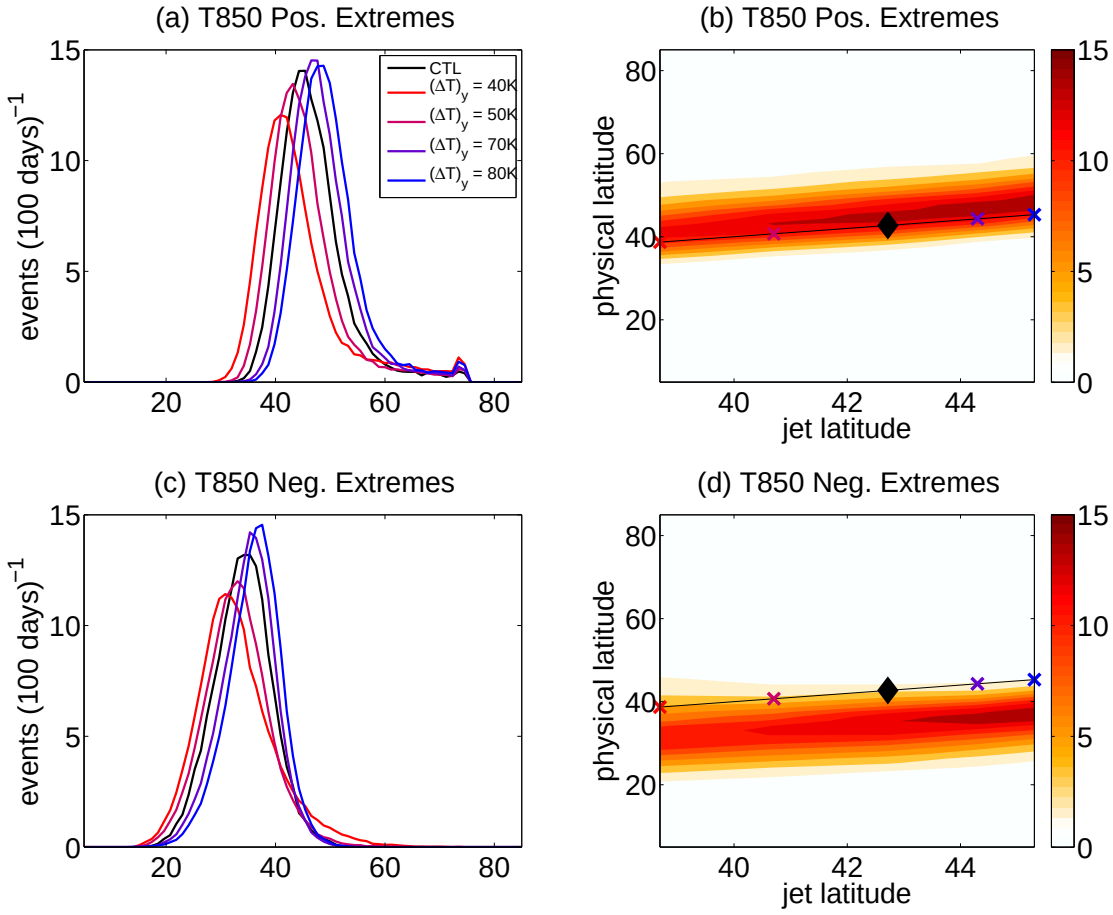

Figure 4.4: The extremes statistics are shown in a similar fashion to Fig. 4.3 with each experiment shown as a contour in the left column and shaded in the right column. Positive extremes are in the top row with negative extremes in the bottom row. Experiments are again stacked at the latitude of the jetstream in the right panel. Colors, markers, and lines are described in Fig. 4.3. The units for the right column are number of events per 100 days with a contour interval of 1.6 events per 100 days.

In a similar fashion to Fig. 4.3, the top row of Fig. 4.4 shows the number of positive (negative) extremes per 100 days in the top (bottom) rows, respectively. Positive extremes occur just on the poleward flank of the jet latitude, while negative extremes occur on the equatorward flank of the jet latitude. From the two panels in the top row, it is clear that with a reduction in the T850 gradient and variability across the midlatitudes with AA, there is also a reduction in the number of extreme events occurring. This is in agreement with the skewness discussed previously. The same can be said about negative extremes where a reduction in negative extremes is associated with an AA signature, although the skewness pattern did not exhibit the same trend. In summary, AA leads to a reduction in the T850 variability that is concurrent with a reduction in the T850 meridional gradient, reduction in jet speed, decrease in jet latitude and reduction in both positive and negative extreme events.

At this point, it would appear that extremes are linearly related to both jet latitude and jet speed and as both jet latitude and speed reduce so do the extremes. So far, the simplest experiments have been analyzed where there is just a simple change to the radiative-equilibrium-temperature profile. It is important to test these results with other thermal perturbations. Continuing to analyze extreme events, the bold TTW runs in Table 2.1 are looked at. Figure 4.5 reproduces Fig. 4.4 but includes the four extra TTW runs. Firstly, the left column demonstrates that as a jetstream is displaced poleward, the extreme events are also shifted poleward indicating that the jetstream's latitude sets the latitude of transition between positive and negative T850 extremes. The right column orders the experiments by jet latitude and plots them as a function of physical latitude and the latitude of the jetstream. Now, focusing just on jet latitude, it appears there is no relationship between the latitude of the jetstream and the number of extreme

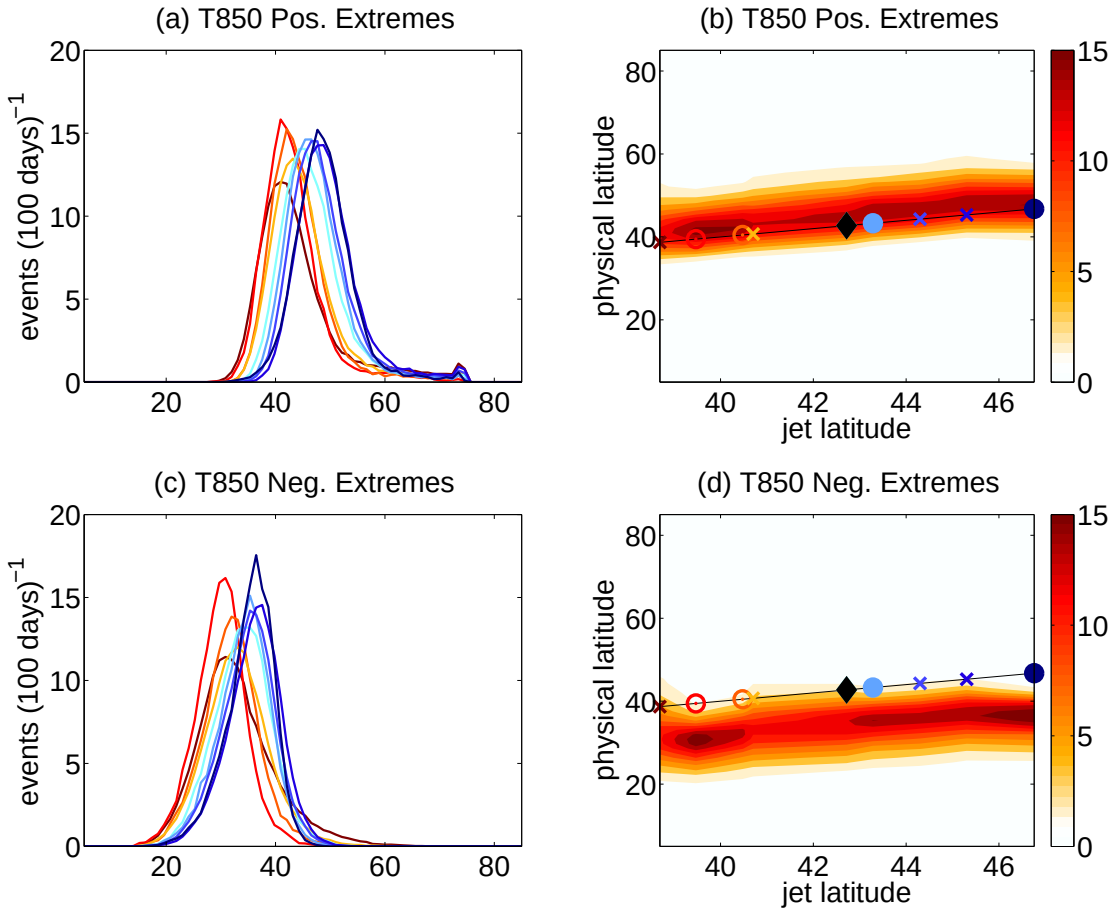

Figure 4.5: Same as Figure 4.4 but the tropical-temperature warming (TTW) runs have been added (see Table 2.1 for details). The TTW runs are added as circles, and the markers and lines are colored by jet latitude, redder lines for equatoward jets and bluer lines for poleward jets. Open circules are the narrow TTW runs, and filled circles are the broad TTW runs. The units for the right column are number of events per 100 days with a contour interval of 1.6 events per 100 days.

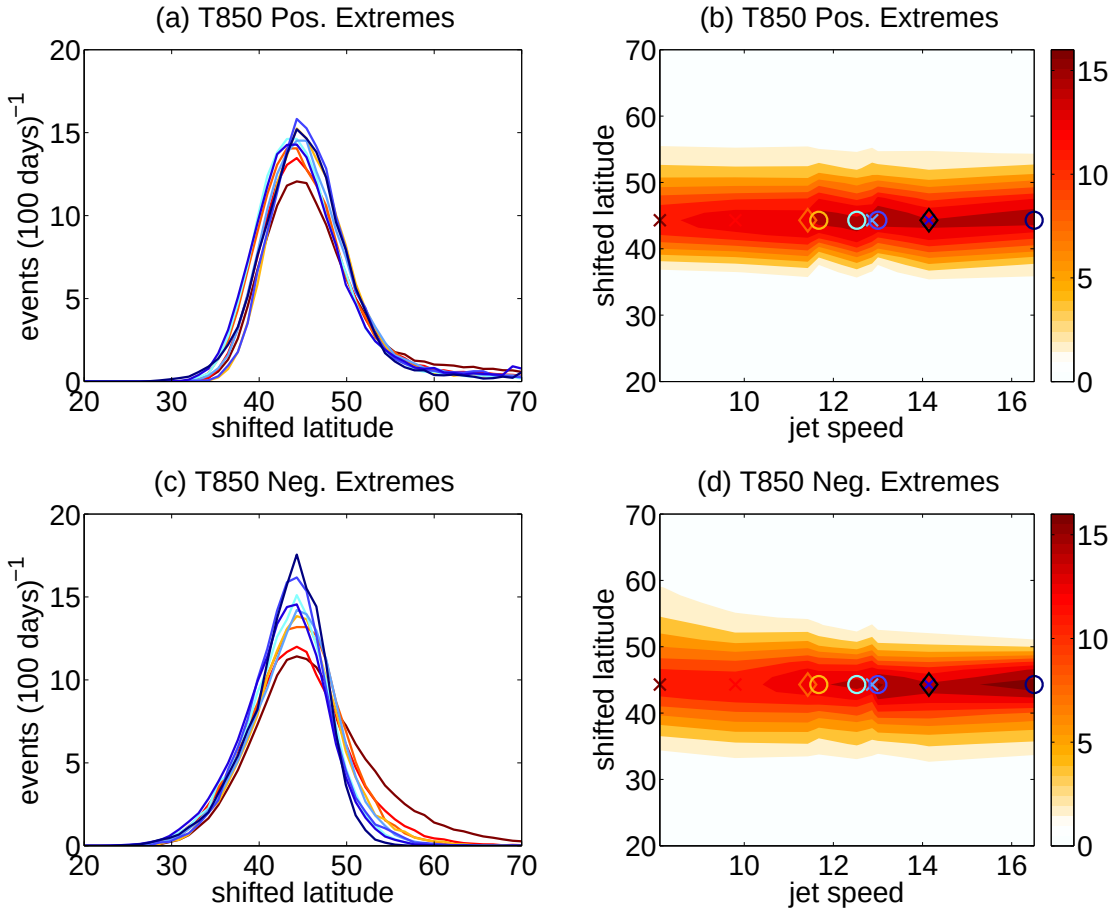

Figure 4.6: Same as Figure 4.5, but the lines in the left column and the experiments in the right column are ordered by jet speed with faster jets in blue and slower jets in red. The maximum in the latitudinal distribution of extreme events are all stacked near 45°. Note the broad TTW runs are not filled here for figure clarity. The units for the right column are number of events per 100 days with a contour interval of 1.6 events per 100 days.

events. The previous relationship between jet latitude, jet speed, and extreme events does not appear when considering other types of thermal perturbations. The same number of events can occur for a jetstream located near 40° and for a jetstream located near 50°. This can be said for both the positive and negative extremes.

The question becomes, why does this relationship break down when considering other thermal perturbations, such as the tropical temperature warming runs described above? In [33, 32], a careful set of numerical experiments is utilized with the express purpose of shifting the jet latitude without changing the speed of the jetstream. This leads to jet latitudes ranging from about 30° to 50° but all with the same speed. Looking more carefully at Fig. 4.5b and d, it becomes apparent that the TTW experiments (especially the low latitude jetstreams near 40°) show more extremes compared with the temperature gradient runs at the same latitude. In contrast to the ΔT runs where strong gradients concur with a poleward jet, the TTW runs here have a strong temperature gradient but an equatorward displaced jetstream. So this suggests that both jet latitude and speed impact the number of extreme events. Figure 4.6 recreates the previous figure. The left column calculates the latitude at which the maximum number of extreme events occur for each experiment. It then centers the latitudes of maximum for each experiment into a central latitude near 45°. The experiments are then colored by jet speed where a bluer color represents a faster jetstream, and a redder color indicates a slower jetstream. Looking at the negative extremes in the first column, a relationship between jet speed and extremes starts to occur. There is a tendency for the slower jetstreams (redder lines) to have less extreme events compared with the faster jetstreams (bluer lines). This can be better seen by arranging all the experiments by jet speed and plotting them in shades. It is now clear that slower jetstreams (experiments to the left in the second column) exhibit fewer extreme events compared with faster jetstreams. There are two effects occurring: as the latitude of the jetstream increases, there is a tendency to increase the number of extreme events. However, an equatorward displaced jetstream may also experience an increase in the number of

spatially and temporally isolated extreme events, if it also has a faster jetstream with more eddy generation and greater variability.

4.3 Summary

This chapter extends the results of [32] and analyzes the response of extreme events to a range of jetstream latitudes and jetstream speeds in an idealized dry, dynamical model from the Geophysical Fluid Dynamics Laboratory. Through the use of two specific thermal perturbations, one altered the equator-to-pole temperature difference, ΔT, and the other placed heating profiles in the tropics, it is shown that the relationship between jet latitude and extreme events from [32] breaks down when a jetstream is displaced equatorward and accelerated. It is this acceleration of the equatorward displaced jetstream that leads to an increase of extreme events for that configuration. Instead of arranging the model runs by jet latitude, these runs were sorted by their jet speed. It is discovered that, no matter the jet latitude, if the jetstream is slow, it has less extreme events, and if a jetstream is fast, it has more extreme events. This both corroborates [32] and extends it to include jet speed.

Further discussions will follow in the final chapter.

CHAPTER 5

BLOCKING

This chapter will continue with the theme of idealized climate change and the response of extreme events, such as blocking, to different thermal perturbations. The first section describes the methodology presented in [42] to describe persistent, anticyclonic geopotential height anomalies. A section is dedicated to results followed by a discussion and summary.

5.1 Method

A second measure is used to quantify persistent anomalies following the blocking algorithm from [42]. The algorithm computes the anomaly from the time- and zonal-mean of the 500 hPa geopotential height (Z500) field at each grid point. This field is then standardized by the maximum of the zonal-mean standard deviation of the Z500 field in time (see Fig. 5.3e). This standardizing value decreases with AA (see values in Fig. 5.3e) implying that the standardized anomalies are increased and are more likely to be considered a block. A threshold is chosen as a sigma level of 1.5. The standardized anomaly field is then analyzed to verify that the anomalies are both spatially large and temporally persistent. 1) First, any point exceeding the given sigma level is stored in a matrix B(t_0,ϕ_0,λ_0). This matrix identifies large magnitude anomalies. 2) The spatial criterion is set by analyzing the surrounding grid points ± about 6° of longitude and latitude. Unlike [42], the grid spacing is not interpolated to 2.8° for concerns this may affect the outcome of the blocking statistics. For this reason, when using the rhomboidally truncated data, the search box may not be

necessarily a square surrounding (t_0,ϕ_0,λ_0). The effect of this has not been analyzed but when looking at these large-scale structures, it should not affect the statistics. A large-scale criterion is satisfied if at least 75% of the surrounding grid points also are in B(t_0,ϕ_0,λ_0) and this point is stored in a matrix S(t_0,ϕ_0,λ_0). 3) After the spatial criterion is met, the temporal criterion needs to be satisfied. If a point, (t_0,ϕ_0,λ_0), is not in S on ($t_0 - 1$,ϕ_0,λ_0) but is in S on (t_0,ϕ_0,λ_0) then S is searched on day $t_0 + 1$. This search forward in time continues until the point is no longer in S (t_0 + lag,ϕ_0,λ_0), at some lag. If lag is greater than or equal to the duration criterion, D, a matrix E is set to 1 from (t_0:t_0 + D -1,ϕ_0,λ_0). Here a duration, D, of 10 days is used. 4) A final criterion requires a reversal in the Z500 field of a least 1 day on the equatorward flank of the block, about 8° to 15° equatorward of the blocked latitude. This reversal criterion will not be used in this analysis to increase the number of events. This will be explained more below.

An example of a typical blocking anticyclone using the above blocking detection method is shown in Fig. 5.1. From left to right, the three panels depict the seven day evolution of a midlatitude block. t_0 represents the initial day that a particular grid point was deemed blocked, namely about 100° longitude and 60° latitude. The block (green contours) is associated with a large-scale anticyclone (black contours and shades) on the poleward flank of the jetstream. On day t_0, the reversal criterion is already satisfied with a large-scale cutoff Z500 contour. By day t_0 + 3, the anticyclone has grown even larger and has a signature of a Rex block [73, 74] with a triplet of low height, high height, to low height. These features remain stagnant and persistent for another three days (and even longer) before eventually decaying toward zonal flow.

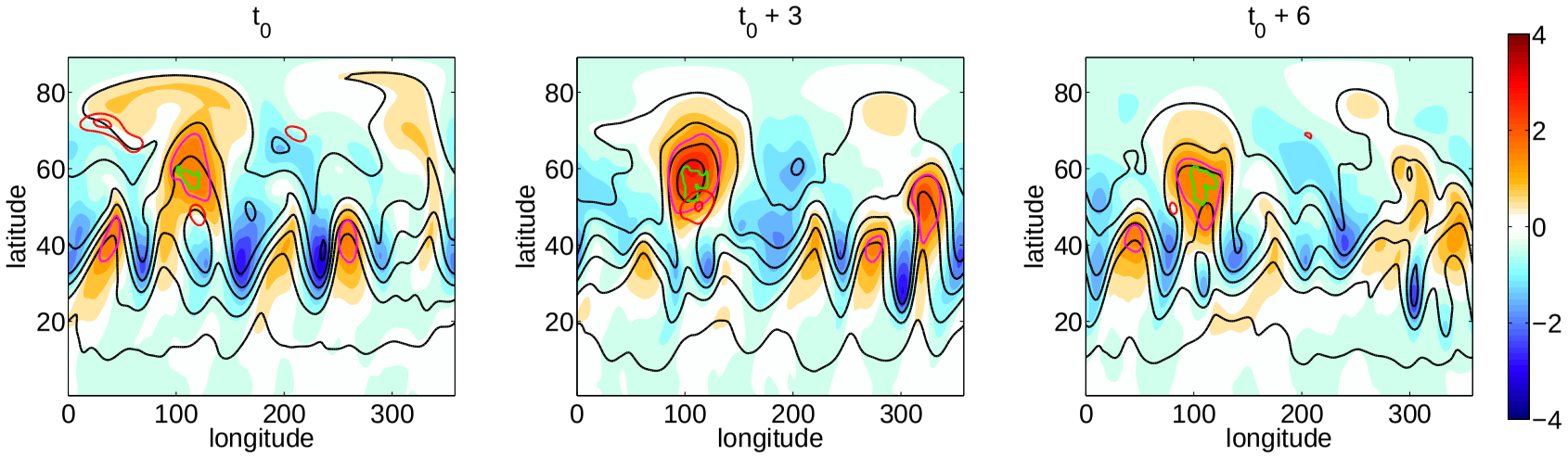

Figure 5.1: The 7 day evolution of a blocking anticyclone as defined in [42] and described in the text. Day t_0 represents the first day that a particular grid point was marked as blocked. The black contours are the Z500 field; shades are time- and zonal-mean Z500 field that has been normalized by the latitudinal maximum in the zonal-mean standard deviation of Z500 (contour interval of 0.4 m); pink contours is the same field but marking when it exceeds a certain sigma value (B matrix in text), 1.5 sigma here; red contours delineate large-scale reversal in the Z500 field.

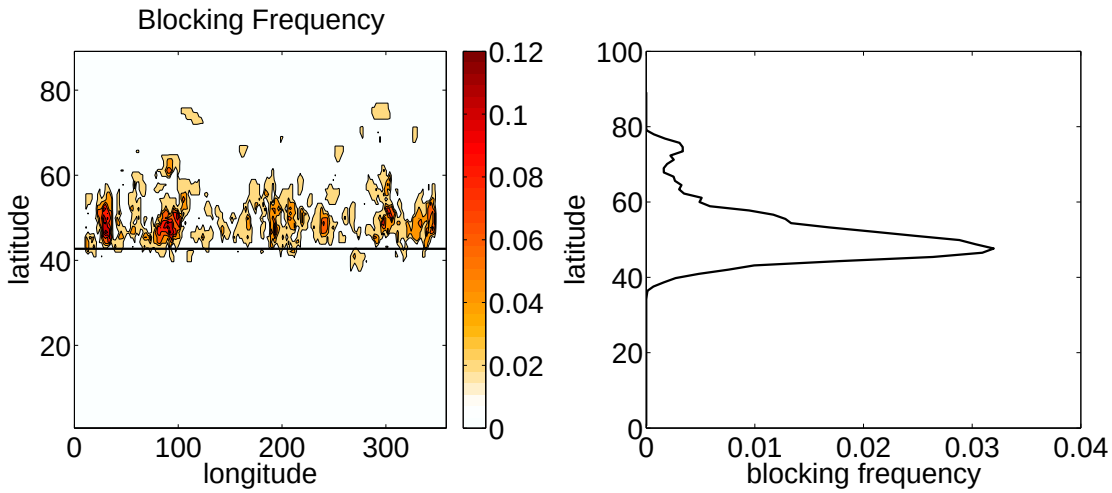

Figure 5.2: Same as Figure 4.2 but for the 500 hPa geopotential height (Z500) statistics using the blocking algorithm from [42]. Blocking frequencies are presented as the percentage (%) of time that a particular point (left panel) is considered blocked and the zonal mean of this quanity (right panel) as the percentage of days that a particular latitude is considered blocked.

Although this blocking diagnostic is applied to anticyclones that are usually associated with warm temperature and ozone extremes, there is still the distinct possibility for a stagnant anticyclone which could produce cold air outbreaks, as is demonstrated in the literature [90, 80]. The winter of 2014 is an example of this situation as a persistent ridge dominated the West coast of the United States for months leading to record deficits in snowfall across the western mountain ranges. This lead to a persistent, strong cold air advection from polar regions to plunge across Canada into the eastern half of the United States e.g. [80]. This same feature is noted in the modeled block where downstream of the block is very strong persistent equatorward advection of colder air, see Fig. 5.1. If this air is able to penetrate the jet latitude into regions of climatologically warm air, a cold extreme may be encountered as easily as a warm extreme associated with

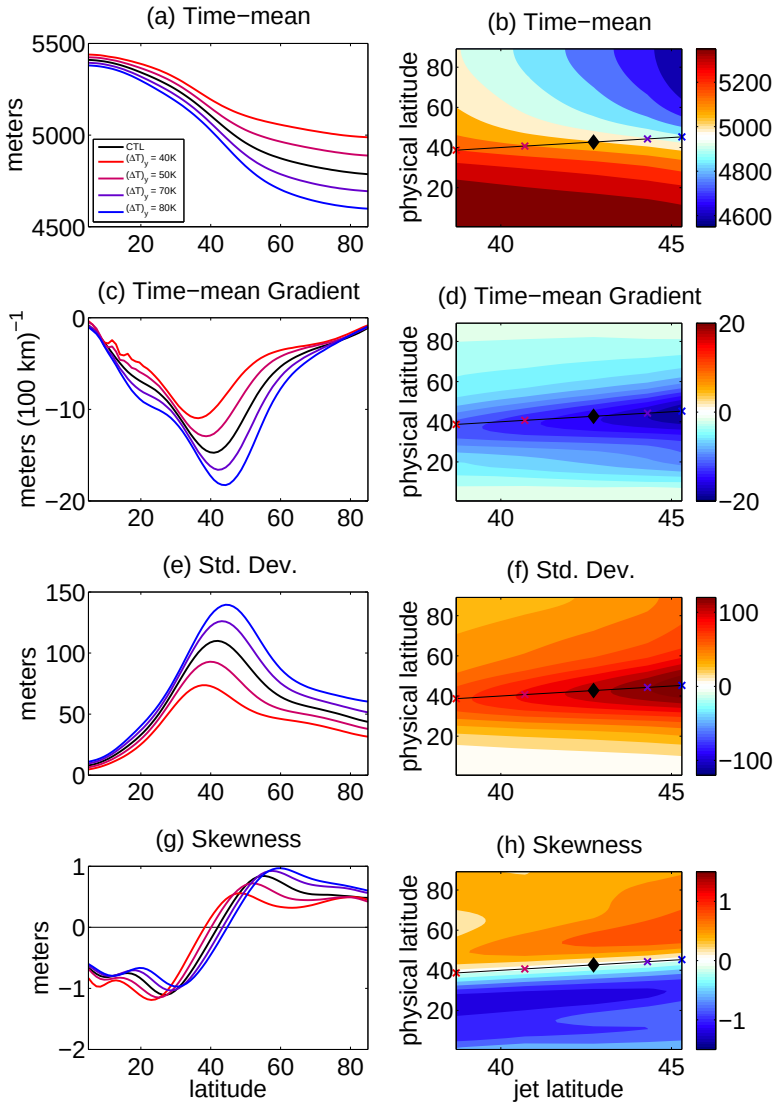

Figure 5.3: Same as Figure 4.3 but for the 500 hPa geopotential height (Z500) statistics. The contour intervals and units for (b) are 80 m, (d) 4 m (100km)$^{-1}$, (f) 24 m and (h) 0.3 m.

poleward advection of warm air on the upstream side of the block. These features, persistent, strong temperature advections, are why blocks have received so much attention in the scientific community, the policy makers, and the general public.

As is done in the previous chapter, Fig. 5.2 depicts the mean statistics associated with the R60 control run simulation. Blocks tend to predominately occur on the poleward flank of the jetstream, as is seen in Fig. 4.2 and occur in regions of warm extremes, where large anticyclones are able to grow without the influence of the jetstream. These extremes have been observed to coincide with large amplitude, quasi-stationary anticyclones and be concurrent with temperature extremes e.g. [14, 27, 66] and ozone events e.g. [92]. The zonal-mean of this panel again shows that the maximum blocked frequency is situated on the poleward flank of the jetstream, much like the warm extremes. The following section will consider the response of blocking frequency to idealized climate change.

5.2 Results

This section will begin with a discussion of the 500 hPa geopotential height (Z500) statistics. These statistics are very similar to the T850 statistics described in the previous chapter but will be described here for completeness. The time-mean Z500 structure in the first row of Fig. 5.3 shows that by decreasing ΔT there are two main responses. Firstly, the entire Z500 structure increases in height, and secondly, the increase in heights are mostly concentrated in the polar region, where heights increase the most. Concurrent with the redistribution of heights across latitudes is a reduction and equatorward shift in the time-mean Z500 meridional gradient with AA (second row of Fig. 5.3). This gradient maximizes just at or slightly equatorward of the climatological jetstream and is nearly halved by reducing ΔT from 80 K to 40 K. This reduction in the meridional gradient coincides with a reduction in the variability of the Z500

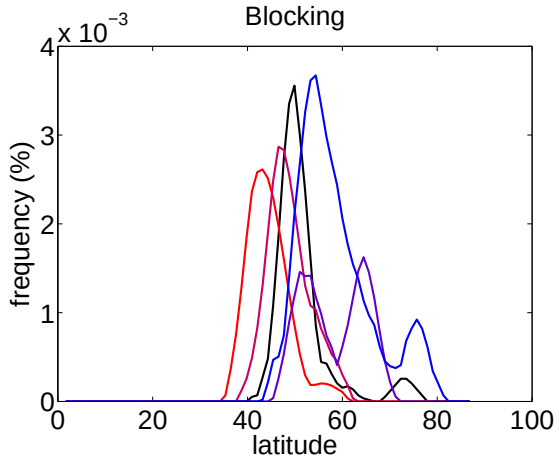

Figure 5.4: The block response is shown in a similar fashion to Fig. 5.3 with each experiment shown as a contour in the left column and shaded in the right column. Colors, markers, and lines are described in Fig. 5.3.

field which also maximizes at or just equatorward of the jet latitude (third row).

On the equatorward flank of the jetstream, the field is negatively skewed indicating regions of low heights associated with cold temperatures. On the poleward flank of the jetstream, the field is positively skewed in regions of warm temperature skewness and warm extremes. As a function of jet latitude, the equatorward flank of the jet indicates a slight reduction in the low height/cold temperature skewness as the jet latitude increases. However, there is a clear increase in Z500 skewness, similar to T850 skewness, on the poleward flank of the jetstream as the jet latitude (and jet speed) increase. These results are consistent with the T850 field and the response of the distributions' tails to changes in jet latitude and jet speed.

Considering the ΔT simulation cases and the control simulation in Fig. 5.4, the blocked frequency is calculated using a value of 1.5 sigma and a duration of

10 days. Similar to the response of extremes to idealized AA, there is a clear reduction in the frequency of persistent anticyclones as ΔT is reduced, consistent with [41]. Along with the reduction in block frequency, there is an equatorward shift in the location of maximum blocked frequency that is situated on the poleward flank of the climatological jet in the right panel. However, sensitivities abound for this blocking defintion, particularly the two threshold requirements. If one relaxes either the duration or threshold criterion by a small amount, say consider a sigma value of 1 and a duration of 8 days, the results are reversed, and AA leads to an increase of smaller amplitude, less persistent events. A transition is occurring as the jet is displaced poleward, where the eddies become not ony stronger but more persistent. It will be these stronger, more persistent events that may lead to an increase in the number of extremes with a faster, more poleward jet location in a future climate.

5.3 Summary

The response of blocking frequency to idealized climate change is analyzed using the Geophysical Fluid Dynamics Laboratory's dry, dynamic atmosphere model. The temperature difference, ΔT, runs are considered, and the value of ΔT is altered from 40 K to 80 K in 10 K increments. ΔT = 40 K produces an Arctic amplification (AA) signature that includes an equatorward shifted, slow jetstream compared with the control run (i.e. ΔT = 60 K). A blocking defintion from [41] is used which describes persistent, anticyclonic 500 hPa geopotential height anomalies. It is shown that associated with this new jetstream configuration, there is a reduction in the frequency of blocking with AA, opposite to [53, 30] and in agreement with [41, 32].

CHAPTER 6

CONCLUSION

This study employs the Geophysical Fluid Dynamics Laboratory's dry, atmospheric dynamical model to examine the effect of climatological jet latitude and jet speed on eddy feedback strengths, annular mode time scales, extreme temperature events, and blocking anticyclones. Idealized thermal perturbations are used to mimic climate responses such as changing the equator-to-pole temperature difference, ΔT, tropical temperature warming (TTW) analogous to ENSO, tropical-upper tropospheric warming (TUW) analogous to greenhouse gas warming, and Arctic surface warming/cooling (ASW/C) analogous to Arctic amplification (AA) [19, 88, 60]. These diabatic perturbations can shift the climatological jet latitude both equatorward and poleward of the [44] system and gives a range of jet latitudes from about 40° to 50°.

Over this range of jet latitudes, it is shown that as the latitude of the jetstream increases, the annular mode decay time scales become smaller and converge toward the observed values [4, 37]. It is also demonstrated that, although there is sensitivity to model resolution and truncation, the R30, R60, T42, and T85 all show this dependence between jet latitude and annular mode decay time scales. Furthermore, a feedback analysis following [84, 70] allows the quantification of feedback strengths that effect the annular mode time scales. Concurrent with the reduction in annular mode time scales, there is a reduction in the eddy momentum forcing and feedback that support a shift in the midlatitude jetstream. Without the support of an eddy feedback, a shifted jetstream cannot support itself against friction and other processes, so it shifts back toward climatology. These high latitude jetstreams (which are predicted to occur with general green-

house warming) may reduce the predictability limit of midlatitude dynamics. This response in the eddy feedback is also shown to be generally consistent across the truncations and resolutions considered here.

Next we diagnose the response of extreme events (both warm and cold extremes) and blocking anticyclones to idealized climate change following methodologies presented in [32] and [41], respectively. First, the response to extremes and blocking is analyzed using model simulations that only changed ΔT. In these runs, ΔT is altered between 40 K and 80 K in 10 K increments where a 40 K run has a strong AA signature. In agreement with [41, 32], it is shown that an AA-like signature leads to an equatorward shifted, slow jetstream, equatorward and weakened eddy fluxes, a reduction in the T850 and Z500 gradients, variabilities (defined as the standard deviation), and skewness, and lastly a reduction in the number of extreme events and blocking frequency. Also, concurrent with an equatorward shifted jetstream is the equatorward shift in both extreme events and blocking where the jetstream sets the transition between cold events on the equatorward flank of the jetstream and warm events on the poleward side of the jetstream with blocking anticyclones also on the poleward flank of the jet. Although it was not done in this analysis, it would be expected that persistent cyclones (defined as persistent, negative Z500 anomalies) would also follow the north-south shift in the climatological jetstream and be situated on the equatorward flank of the jet. This may not be the case though, as many cyclones persist for many days in the subpolar regions, especially in the lower resolved models.

6.1 Discussion

Through a Fourier spectral decomposition, [41] shows that an idealized AA signature leads to a reduction in the meridional wave amplitudes, which are the north-south wave amplitudes associated with blocking-like wave structures. Using the recently developed finite-amplitude wave activity [69] (presented in Chapter 2), a similar conclusion can be drawn and is illustrated in Fig. 6.1. Consistent with a reduction in the number of warm and cold extremes with AA and a reduction of blocking anticyclones with AA, there is a large reduction in wave amplitudes at all latitudes and especially at the latitude of the jetstream. Both panels demonstrate that as the Arctic regions heat faster than the equatorial and midlatitude regions, a reduction in wave amplitudes occurs which is consistent with a reduction in the T850 skewness, extreme events, Z500 skewness, and blocking anticyclones. Independent to model resolution and truncation, to blocking definition, to duration criterion, to block amplitude, to block size, etc. by just looking at the climatological wave amplitudes, one can deduce the response to extreme events and blocking. Considering the length of time it takes to compute these quantities, especially the blocking algorithm, it would save considerable computation time and personal time to instead compute the time-mean wave activity. On the negative side, the time-mean wave activity does not provide details of blocking dynamics, block size, or block duration.

This point can be further elucidated and simplified by considering the meridional T850 profile. The majority of this thesis has been dedicated to describing profiles of T850 and extreme events by the latitude or speed of the eddy-driven jetstream. Taking one step back, Fig. 6.2 plots two quantities that summarize the T850 gradient profile. The magnitude of the T850 gradient is

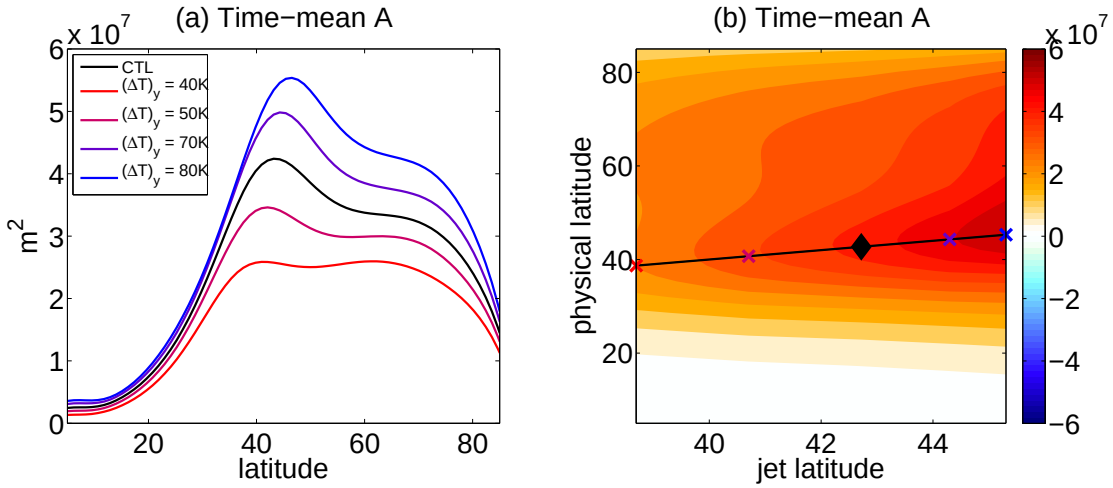

Figure 6.1: (a) Time-mean finite-amplitude wave activity, A, as contour plots for each ΔT run and (b) a shaded plot that combines each experiment as a function of physical latitude and experimental jet latitude. Markers and colors are the same as Fig. 4.3.

calculated as the maximum value in Fig. 4.3 for each simulation. The latitude of this maximum is taken as the latitude of maximum T850 gradient. These values are plotted as a function of jet latitude and jet speed in Fig. 6.2. Note the only runs shown here are the ΔT runs. For this particular set of simulations, it is important to recognize that as the latitude of the jet increases, the speed of the jet linearly increases. So for this reason, all of the correlations (presented as floating numbers in each panel) are nearly one. So as the baroclinic zone (and hence the jetstream) shifts poleward, it also strengthens and supports a faster jetstream with more extreme events (Fig. 4.4) and more blocking (Fig. 5.4).

However, this is not the case when considering a strengthened baroclinic zone that shifts the jet latitude equatorward. Figure 6.3 now considers the R60 TTW runs. In these TTW runs, a narrow TTW profile actually strengthens the baroclinic zone and shifts the jet equatorward, opposite to angular momentum

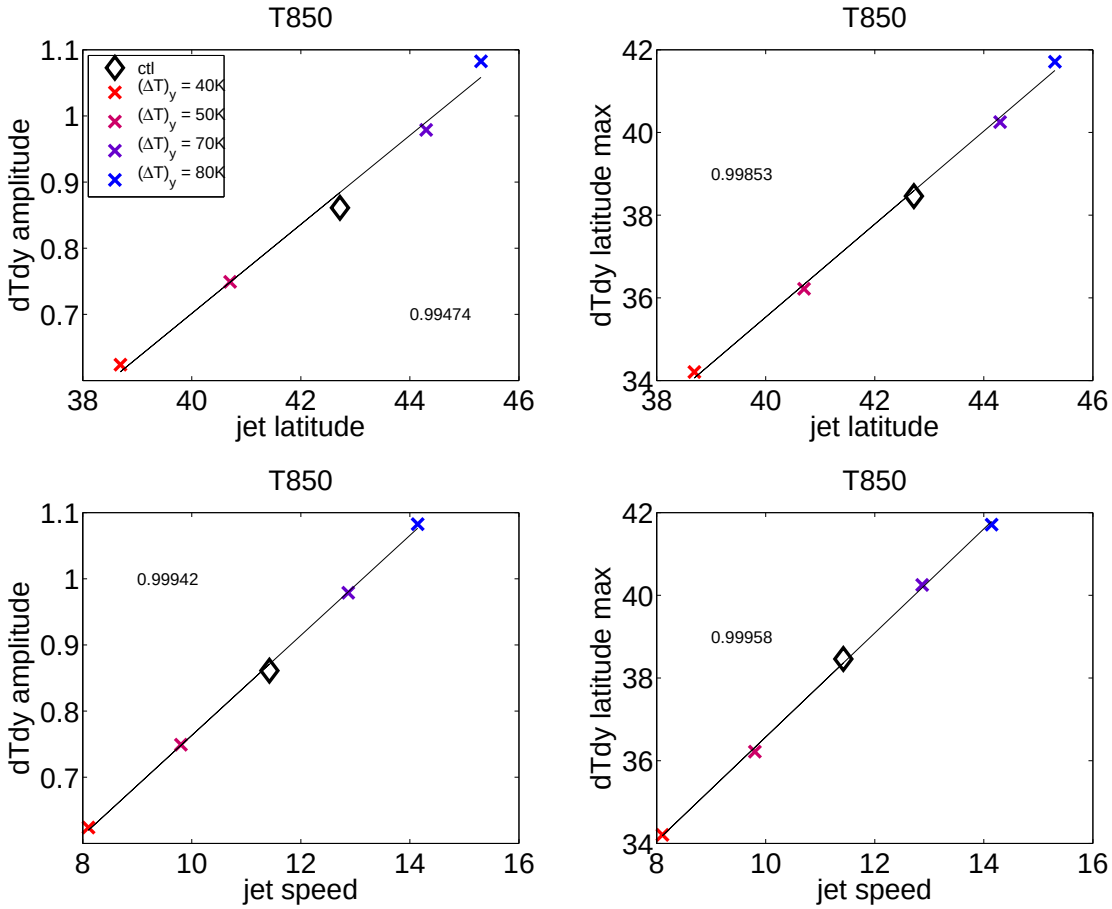

Figure 6.2: Top row: the amplitude of the maximum value of the T850 meridional gradient (dTdy) (left panel) and latitude of this maximum value (right panel) as a function of climatological jet latitude. Bottom row: the same T850 gradient values but as a function of jet speed. Markers and colors are the same as Fig. 4.3. Correlation coefficients are shown as floating numbers for each respective panel.

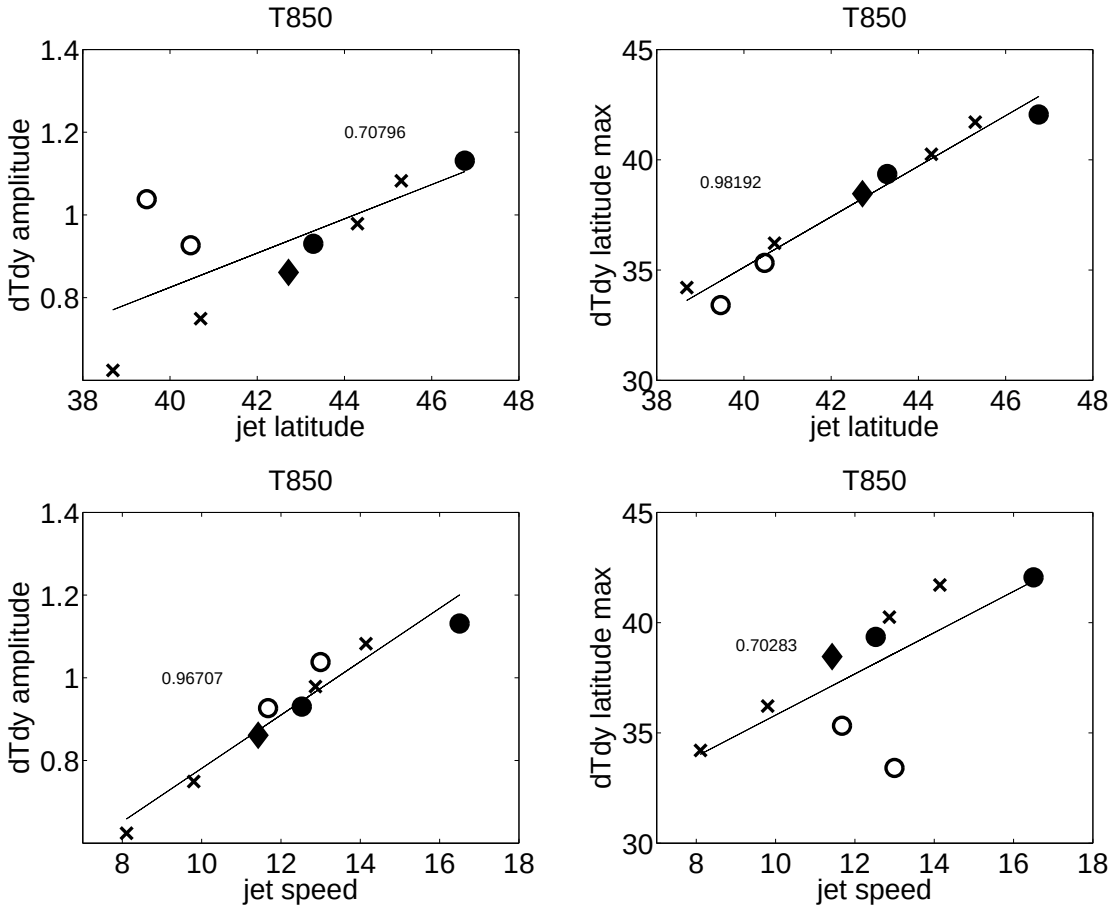

Figure 6.3: Same as Fig. 6.2 but the tropical temperature warming (TTW) runs have also been added. Colors have been removed. Circles represent the TTW runs, x's the ΔT runs, and the diamond is the control run. Closed circles indicate the broad TTW runs.

considerations but consistent with the Pacific Ocean's merged subtropical and eddy-driven jet at 30° with a speed of nearly 50 m s^{-1} [28]. The panels in Fig. 6.3 are the same as in Fig. 6.2. It clarifies the mechanisms that set the jetstream characteristics, i.e. jet latitude and jet strength. There is no longer a strong relationship between the amplitude of the T850 gradient and the jet latitude and a weaker relationship between the latitude of the maximum T850 gradient and the jet speed. In [41], the only experiments considered are the ΔT runs shown

in Fig. 6.2. In these runs, as mentioned above, the relationship between jet latitude and jet speed is linear. In [33, 32], the model experiments are carefully designed such that the latitude of the eddy-driven jet could be altered without altering the speed of the jetstream itself. Both papers show the same results that with an increase in jet latitude, there is an increase in both the number of persistent anomaly signatures (blocks) and the number of isolated extremes events. However, neither report considers the case where an equatorward displaced jetstream is stronger than a poleward displaced jetstream. The current results shown here both corroborate these results and extend these results to consider both changes in jet latitude and jet speed.

In order to conserve computing space and time, the TTW, TUW, ASW/C, and ΔT runs were initially conducted at an R30 resolution in order to produce a wide variety of thermal perturbation structures, thermal perturbation strengths, and jet latitudes. To test the robustness of the results, a subset of TTW simulations are performed at R60, T42 and T85 truncation and resolution. The annular mode time scale and feedback results were corroborated with the higher resolution simulations. However, when beginning the analysis of extreme events from [32], the results were not reproducible. Deciding that resolution may be the issue, the ΔT runs were rerun at the R60 truncation level for extreme events, and now the results from [32] were reproduced. The main results presented in Fig. 4.6 are recreated with the R30 data utilizing the TTW, TUW, ASW/C, and ΔT runs in Fig. 6.4. Again, the latitudinal profile of extremes is stacked at a single latitude and the colors indicate the jet speed (red for slow and blue for fast). It becomes very evident in the right panel of the figure that there appears to be a maximum in extreme events for jets with an intermediate speed, and that both slower and faster jets have less extreme events. This feature needs to be noted

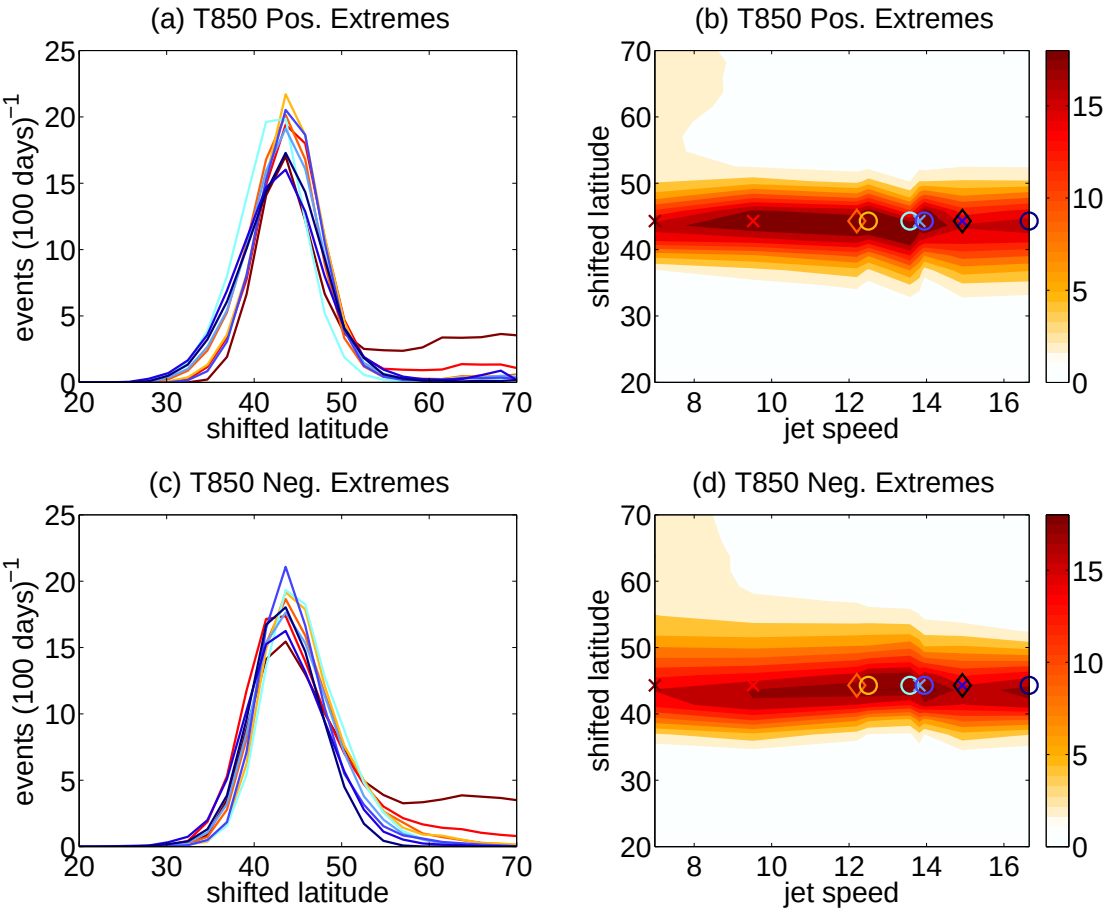

Figure 6.4: Same as Fig. 4.6 but for the R30 simulations. Included in the plots are the tropical temperature warming (TTW) runs (circles), the tropical-upper tropospheric (TUW) runs (triangles), the Arctic surface warming/cooling (ASW/C) runs (stars), and the ΔT runs (x's). For figure clarity, the broad TTW and TUW runs have not been filled. The contour interval and unit for the right column are 2 events per 100 days.

to use caution when looking at low resolved models. For these experiments, selecting a few simulations with more poleward and equatorward jet latitudes to verify results is warranted.

6.2 Future Work

Nearly 15 years ago, the first and second mode of midlatitude variability were analyzed using principal component analysis [56]. The first mode represents the north-south fluctuation in the jetstream, the annular modes. The second mode describes the strengthening and weakening of the jetstream. This mode of variability is shown to not exhibit an eddy momentum feedback demonstrating that the eddy feedback is essential for developing the first mode of variability, i.e. the annular modes. The second mode of variability accounts for the strengthening and weakening of the eddy-driven jetstream in the Southern Hemisphere [56]. If the research presented in this thesis using an idealiezd model are realizable in the observations, this implies that the second mode of variability may be intimately linked to extreme events and blocking. Since the annular mode has time scales near 6 to 20 days, it comes out as the leading mode of variability. Blocking has time scales of 4 to 8 days, about half the time scale of the annular mode. It seems fitting that blocking may come out as the second mode of variability. This would provide a succinct physical interpretation of both modes of variability.

In order to determine the relevance of this work to the real world, it would be important to test these ideas using the observations and further extend them to CMIP runs. Firstly, it would be good to verify these results in observations. A methodology will be suggested here. Consider the Atlantic basin and the cor-

responding North Atlantic Oscillation, which describes the north-south fluctuation of the eddy-driven jetstream. The jetstream is classically characterized by its latitude and speed. To test the proposed hypothesis in this paper, one could take the top and bottom 1% of the jet latitudes and jet speeds and determine the probability that blocking is occuring in certain regions across the Atlantic, e.g. the Greenland blocking region or the European blocking region. My expectations are two fold. Considering jet latitude and jet speed separately, I would expect that if jet latitude is high and jet speed is normal that there would be enhanced slow moving weather systems due to enhanced variability, as shown with modeling efforts in [32]. On the other hand, if jet latitude is normal and jet speed is high, I would also expect increased slow moving weather systems, as shown with modeling efforts in [42]. The Pacific jetstream exhibits both an equatorward located jetstream (near 30°), a very fast jetstream (nearly 50 m s^{-1}), and a merged subtropical and eddy-driven jetstream [28]. In this situation, it would be a balancing act between equatorward jetstreams and less extremes and fast jetstreams and more extremes. If this is the case, I would expect the jet speed to be the dominating factor, where the faster the jet speed, the more slow moving weather systems develop, again due to the enhanced variability.

BIBLIOGRAPHY

[1] Ara Arakelian and Francis Codron. Southern Hemisphere Jet Variability in the IPSL GCM at varying Resolutions. *Journal of the Atmospheric Sciences*, page 120723051252008, 2012.

[2] Mark P. Baldwin and T J Dunkerton. Stratospheric harbingers of anomalous weather regimes. *Science (New York, N.Y.)*, 294(5542):581–584, 2001.

[3] Mark P. Baldwin, David B. Stephenson, and Ian T. Jolliffe. Spatial weighting and iterative projection methods for EOFs. *Journal of Climate*, 22(2):234–243, jan 2009.

[4] Mark P. Baldwin, David B Stephenson, David W. J. Thompson, Timothy J Dunkerton, Andrew J Charlton, and Alan O'Neill. Stratospheric memory and skill of extended-range weather forecasts. *Science (New York, N.Y.)*, 301(5633):636–640, 2003.

[5] Elizabeth A. Barnes and Dennis L. Hartmann. Testing a theory for the effect of latitude on the persistence of eddy-driven jets using CMIP3 simulations. *Geophysical Research Letters*, 37, aug 2010.

[6] Elizabeth A. Barnes, Dennis L. Hartmann, Dargan M. W. Frierson, and Joseph Kidston. Effect of latitude on the persistence of eddy-driven jets. *Geophysical Research Letters*, 37:1–5, jun 2010.

[7] Elizabeth A. Barnes and Lorenzo M. Polvani. Response of the midlatitude jets, and of their variability, to increased greenhouse gases in the CMIP5 models. *Journal of Climate*, 26(18):7117–7135, sep 2013.

[8] Elizabeth A. Barnes, Lorenzo M. Polvani, and Adam H Sobel. Model projections of atmospheric steering of Sandy-like superstorms. *Proceedings of the National Academy of Sciences of the United States of America*, 110(38):15211–5, 2013.

[9] Elizabeth A. Barnes and James a. Screen. The impact of Arctic warming on the midlatitude jet-stream: Can it? Has it? Will it? *Wiley Interdisciplinary Reviews: Climate Change*, 6(3):277–286, 2015.

[10] Elizabeth A. Barnes, Julia Slingo, and Tim J. Woollings. A methodology for the comparison of blocking climatologies across indices, models and climate scenarios. *Climate Dynamics*, 38(11-12):2467–2481, 2012.

[11] Elizabeth A. Barnes and David W. J. Thompson. Comparing the Roles of Barotropic versus Baroclinic Feedbacks in the Atmosphere's Response to Mechanical Forcing. *Journal of the Atmospheric Sciences*, 71(1):177–194, jan 2014.

[12] David Barriopedro, Ricardo García-Herrera, Anthony R. Lupo, and Emiliano Hernández. A climatology of Northern Hemisphere blocking. *Journal of Climate*, 19(6):1042–1063, 2006.

[13] James J. Benedict, Sukyoung Lee, and Steven B. Feldstein. Synoptic View of the North Atlantic Oscillation. *Journal of the Atmospheric Sciences*, 61(2):121–144, jan 2004.

[14] Robert X. Black and Brent a. McDaniel. Diagnostic case studies of the northern annular mode. *Journal of Climate*, 17(20):3990–4004, 2004.

[15] Roxana Bojariu and Luis Gimeno. Predictability and numerical modelling of the North Atlantic Oscillation. *Earth-Science Reviews*, 63(1-2):145–168, oct 2003.

[16] Tania Buehler, Christoph C. Raible, and Thomas F. Stocker. The relationship of winter season North Atlantic blocking frequencies to extreme cold or dry spells in the ERA-40. *Tellus A*, 63(2):212–222, mar 2011.

[17] D. Alex Burrows, Gang Chen, and Lantao Sun. Barotropic and Baroclinic Eddy Feedbacks in the Midlatitude Jet Variability and Responses to Climate ChangeLike Thermal Forcings: accepted to JAS. 2016.

[18] Neal Butchart and Ellis E. Remsberg. The area of the stratospheric polar vortex as a diagnostic for tracer transport on an isentropic surface. *Journal of the Atmospheric Sciences*, 43(13):1319–1339, 1986.

[19] Amy H. Butler, David W. J. Thompson, and Ross Heikes. The Steady-State Atmospheric Circulation Response to Climate Changelike Thermal Forcings in a Simple General Circulation Model. *Journal of Climate*, 23(13):3474–3496, jul 2010.

[20] Gang Chen, Jian Lu, D. Alex Burrows, and Ruby L. Leung. Local Finite-amplitude Wave Activity as a Diagnostic of Anomalous Weather Events. *Geophysical Research Letters*, 2015.

[21] Gang Chen and Alan R. Plumb. Quantifying the Eddy Feedback and the

Persistence of the Zonal Index in an Idealized Atmospheric Model. *Journal of the Atmospheric Sciences*, 66(12):3707–3720, dec 2009.

[22] Gang Chen and Pablo Zurita-Gotor. The Tropospheric Jet Response to Prescribed Zonal Forcing in an Idealized Atmospheric Model. *Journal of the Atmospheric Sciences*, 65(7):2254–2271, jul 2008.

[23] Dim Coumou and S Rahmstorf. A decade of weather extremes. *Nature Climate Change*, 2(7):491–496, 2012.

[24] Mischa Croci-Maspoli, Cornelia Schwierz, and H. C. Davies. A multifaceted climatology of atmospheric blocking and its recent linear trend. *Journal of Climate*, 20(4):633–649, 2007.

[25] Marie-Estelle Demory, Pier Luigi Vidale, Malcolm J. Roberts, Paul Berrisford, Jane Strachan, Reinhard Schiemann, and Matthew S. Mizielinski. The role of horizontal resolution in simulating drivers of the global hydrological cycle. *Climate Dynamics*, 42(7-8):2201–2225, 2014.

[26] Randall M. Dole and Neil D. Gordon. Persistent anomalies of the extratropical Northern Hemisphere wintertime circulation - Structure. *Monthly Weather Review*, 111:1567–1586, 1983.

[27] Randall M. Dole, Martin P Hoerling, Judith Perlwitz, Jon Eischeid, Philip Pegion, Tao Zhang, Xiao-Wei Quan, Taiyi Xu, and Donald Murray. Was there a basis for anticipating the 2010 Russian heat wave? *Geophysical Research Letters*, 38(6), mar 2011.

[28] Scott J. Eichelberger and Dennis L. Hartmann. Zonal jet structure and the leading mode of variability. *Journal of Climate*, 20(20):5149–5163, 2007.

[29] Steven B. Feldstein and Sukyoung Lee. Is the Atmospheric Zonal Index Driven by an Eddy Feedback? *Journal of the Atmospheric Sciences*, 55(19):3077–3086, oct 1998.

[30] Jennifer a. Francis and Stephen J. Vavrus. Evidence linking Arctic amplification to extreme weather in mid-latitudes. *Geophysical Research Letters*, 39(6):n/a–n/a, mar 2012.

[31] Christian L. E. Franzke, Sukyoung Lee, and Steven B. Feldstein. Is the North Atlantic Oscillation a Breaking Wave? *Journal of the Atmospheric Sciences*, 61(2):145–160, jan 2004.

[32] Chaim I. Garfinkel and Nili Harnik. The non-Gaussianity and spatial asymmetry of temperature extremes relative to the storm track: the role of horizontal advection. *Journal of Climate*, (August):JCLI–D–15–0806.1, 2016.

[33] Chaim I. Garfinkel, Darryn W. Waugh, and Edwin P. Gerber. The Effect of Tropospheric Jet Latitude on Coupling between the Stratospheric Polar Vortex and the Troposphere. *Journal of Climate*, pages 2077–2095, sep 2013.

[34] Edwin P. Gerber, Lorenzo M. Polvani, and D. Ancukiewicz. Annular mode time scales in the Intergovernmental Panel on Climate Change Fourth Assessment Report models. *Geophysical Research Letters*, 35(L22707):1–5, nov 2008.

[35] Edwin P. Gerber and Geoffrey K. Vallis. A Stochastic Model for the Spatial Structure of Annular Patterns of Variability and the North Atlantic Oscillation. *Journal of climate*, 18:2102–2119, 2005.

[36] Edwin P. Gerber and Geoffrey K. Vallis. Eddy-zonal flow interactions and the persistence of the zonal index. *Journal of the Atmospheric Sciences*, 64(9):3296–3311, sep 2007.

[37] Edwin P. Gerber, Sergey Voronin, and Lorenzo M. Polvani. Testing the Annular Mode Autocorrelation Time Scale in Simple Atmospheric General Circulation Models. *Monthly Weather Review*, 136(4):1523–1536, apr 2008.

[38] Nathan P Gillett and David W. J. Thompson. Simulation of recent southern hemisphere climate change. *Science (New York, N.Y.)*, 302(October):273–275, 2003.

[39] Tingting Gong, Steven B. Feldstein, and Dehai Luo. The Impact of ENSO on Wave Breaking and Southern Annular Mode Events. *Journal of the Atmospheric Sciences*, 67(9):2854–2870, sep 2010.

[40] Dennis L. Hartmann. The Atmospheric General Circulation and Its Variability. 85:123–143, 2007.

[41] Pedram Hassanzadeh and Zhiming Kuang. Blocking variability: Arctic Amplification versus Arctic Oscillation. *Geophysical Research Letters*, 42(20):8586–8595, 2015.

[42] Pedram Hassanzadeh, Zhiming Kuang, and Brian F. Farrell. Responses of midlatitude blocks and wave amplitude to changes in the meridional temperature gradient in an idealized dry GCM. *Geophysical Research Letters*, 41(14):5223–5232, jul 2014.

[43] Gabriele C. Hegerl, Thomas J. Crowley, Myles Allen, William T. Hyde, Henry N. Pollack, Jason Smerdon, and Eduardo Zorita. Detection of human influence on a new, validated 1500-year temperature reconstruction. *Journal of Climate*, 20(4):650–666, 2007.

[44] Isaac M. Held and Max Suarez. A proposal for the intercomparison of the dynamical cores of atmospheric general circulation models. *Bulletin of the American Meteorological Society*, 75(10):1825–1830, 1994.

[45] James W. Hurrell. Decadal trends in the North Atlantic Oscillation: regional temperatures and precipitation. *Science*, 269(5224):676–679, 1995.

[46] Thomas Jung, M. J. Miller, TN Palmer, P. Towers, N. Wedi, D. Achuthavarier, J. M. Adams, E. L. Altshuler, B. A. Cash, J. L. Kinter, L. Marx, C. Stan, and K. I. Hodges. High-Resolution Global Climate Simulations with the ECMWF Model in Project Athena: Experimental Design, Model Climate, and Seasonal Forecast Skill. *Journal of Climate*, 25(9):3155–3172, 2012.

[47] V. V. Kharin, F. W. Zwiers, X. Zhang, and M. Wehner. Changes in temperature and precipitation extremes in the CMIP5 ensemble. *Climatic Change*, 119(2):345–357, 2013.

[48] Joseph Kidston, D. M. W. Frierson, J. A. Renwick, and Geoffrey K. Vallis. Observations, Simulations, and Dynamics of Jet Stream Variability and Annular Modes. *Journal of Climate*, 23:6186–6199, dec 2010.

[49] Paul J. Kushner, Isaac M. Held, and Thomas L. Delworth. Southern Hemisphere atmospheric circulation response to global warming. *Journal of Climate*, 14:2238–2249, 2001.

[50] Sukyoung Lee and Steven B. Feldstein. Mechanism of zonal index evolution in a two-layer model. *Journal of the Atmospheric Sciences*, 53(15):2232–2246, 1996.

[51] C. E. Leith. Climate response and fluctuation dissipation. *Journal of the Atmospheric Sciences*, 32:2022–2026, 1975.

[52] Michelle L. L'Heureux and David W. J. Thompson. Observed relationships between the El Nino-Southern Oscillation and the extratropical zonal-mean circulation. *Journal of Climate*, 19:276–288, 2006.

[53] Jiping Liu, Judith a Curry, Huijun Wang, Mirong Song, and Radley M Horton. Impact of declining Arctic sea ice on winter snowfall. *Proceedings of the National Academy of Sciences*, 109(11):4074–9, 2012.

[54] David J. Lorenz. Understanding Midlatitude Jet Variability and Change Using Rossby Wave Chromatography: Poleward-Shifted Jets in Response to External Forcing. *Journal of the Atmospheric Sciences*, 71(7):2370–2389, jul 2014.

[55] David J. Lorenz and Eric T. DeWeaver. Tropopause height and zonal wind response to global warming in the IPCC scenario integrations. *Journal of Geophysical Research: Atmospheres*, 112(10):1–11, 2007.

[56] David J. Lorenz and Dennis L. Hartmann. Eddy-zonal flow feedback in the Southern Hemisphere. *Journal of the Atmospheric Sciences*, 58:3312–3327, 2001.

[57] David J. Lorenz and Dennis L. Hartmann. Eddy-zonal flow feedback in the Northern Hemisphere winter. *Journal of Climate*, 16:1212–1227, 2003.

[58] Jian Lu, Gang Chen, and Dargan M. W. Frierson. Response of the Zonal Mean Atmospheric Circulation to El Niño versus Global Warming. *Journal of Climate*, 21(22):5835–5851, nov 2008.

[59] Jian Lu, Gang Chen, Ruby L. Leung, D. Alex Burrows, Yang Qing, Sakaguchi Koichi, and Hagos Samson. Toward the Dynamical Convergence on the Jet Stream in Aquaplanet AGCMs. *Journal of Climate*, 28(17):6763–6782, 2015.

[60] Jian Lu, Lantao Sun, Yutian Wu, and Gang Chen. The Role of Subtropical Irreversible PV Mixing in the Zonal Mean Circulation Response to Global WarmingLike Thermal Forcing. *Journal of Climate*, 27(6):2297–2316, mar 2014.

[61] Jian Lu, Gabriel A. Vecchi, and Thomas Reichler. Expansion of the Hadley cell under global warming. *Geophysical Research Letters*, 34(6):L06805, mar 2007.

[62] Syukuro Manabe and Richard T. Wetherald. Thermal Equilibrium of the Atmosphere with a Given Distribution of Relative Humidity, 1967.

[63] Gareth J. Marshall. Trends in the Southern Annular Mode from observations and reanalyses. *Journal of Climate*, 16(24):4134–4143, 2003.

[64] Olivia Martius, Cornelia Schwierz, and H. C. Davies. Breaking Waves at the Tropopause in the Wintertime Northern Hemisphere: Climatological Analyses of the Orientation and the Theoretical LC1/2 Classification. *Journal of the Atmospheric Sciences*, 64(7):2576–2592, jul 2007.

[65] G. Masato, B. J. Hoskins, and T. J. Woollings. Wave-breaking characteristics of midlatitude blocking. *Quarterly Journal of the Royal Meteorological Society*, 138(666):1285–1296, 2012.

[66] Mio Matsueda. Predictability of Euro-Russian blocking in summer of 2010. *Geophysical Research Letters*, 38(6):1–6, 2011.

[67] Mio Matsueda, Ryo Mizuta, and Shoji Kusunoki. Future change in wintertime atmospheric blocking simulated using a 20-km-mesh atmospheric global circulation model. *Journal of Geophysical Research: Atmospheres*, 114(12):1–10, 2009.

[68] Clio Michel and Gwendal Rivière. The Link between Rossby Wave Breakings and Weather Regime Transitions. *Journal of the Atmospheric Sciences*, 68(8):1730–1748, 2011.

[69] Noboru Nakamura and Da Zhu. Finite-Amplitude Wave Activity and Diffusive Flux of Potential Vorticity in EddyMean Flow Interaction. *Journal of the Atmospheric Sciences*, 67(9):2701–2716, sep 2010.

[70] Yu Nie, Yang Zhang, Gang Chen, Xiu-Qun Yang, and D. Alex Burrows. Quantifying barotropic and baroclinic eddy feedbacks in the persistence of the Southern Annular Mode. *Geophysical Research Letters*, pages 1–25, 2014.

[71] Judith Perlwitz, Steven Pawson, Ryan L. Fogt, J. Eric Nielsen, and William D. Neff. Impact of stratospheric ozone hole recovery on Antarctic climate. *Geophysical Research Letters*, 35(8):L08714, apr 2008.

[72] Thomas C. Peterson, Martin P Hoerling, Peter A Stott, and Stephanie C

Herring. Explaining Extreme Events of 2012 from a Climate Perspective. *Bulletin of the American Meteorological Society*, 94(9):S6–S9, 2013.

[73] Daniel F. Rex. Blocking Action in the Middle Troposphere and its Effect upon Regional Climate. I. An Aerological Study of Blocking Action. *Tellus*, 2:196–211, 1950.

[74] Daniel F. Rex. Blocking Action in the middle troposphere and its effect upon regional climate. II. The climatology of blocking action. *Tellus*, 2(October):275–301, 1950.

[75] Michael J. Ring and Alan R. Plumb. The Response of a Simplified GCM to Axisymmetric Forcings: Applicability of the FluctuationDissipation Theorem. *Journal of the Atmospheric Sciences*, 65(12):3880–3898, dec 2008.

[76] Walter A. Robinson. A Baroclinic Mechanism for the Eddy Feedback on the Zonal Index. *Journal of the Atmospheric Sciences*, 57(3):415–422, feb 2000.

[77] Ju Mee Ryoo, Yohai Kaspi, Darryn W. Waugh, George N. Kiladis, Duane E. Waliser, Eric J. Fetzer, and Jinwon Kim. Impact of rossby wave breaking on U.S. west coast winter precipitation during ENSO events. *Journal of Climate*, 26(17):6360–6382, 2013.

[78] Cornelia Schwierz, Mischa Croci-Maspoli, and H. C. Davies. Perspicacious indicators of atmospheric blocking. *Geophysical Research Letters*, 31(L06125), 2004.

[79] James a. Screen. Arctic amplification decreases temperature variance in northern mid- to high-latitudes. *Nature Climate Change*, 4(7):577–582, 2014.

[80] James a. Screen, Clara Deser, and Lantao Sun. Reduced Risk of North American Cold Extremes due to Continued Arctic Sea Ice Loss. *Bulletin of the American Meteorological Society*, 96(9):1489–1503, 2015.

[81] James A. Screen and Ian Simmonds. The central role of diminishing sea ice in recent Arctic temperature amplification. *Nature*, 464(7293):1334–1337, 2010.

[82] James a. Screen and Ian Simmonds. Exploring links between Arctic amplification and mid-latitude weather. *Geophysical Research Letters*, 40(5):959–964, 2013.

[83] Richard Seager and David S. Battisti. Challenges to Our Understanding of the General Circulation: Abrupt Climate Change. In *The Global Circulation of the Atmosphere*. 2007.

[84] Isla R. Simpson, Theodore G. Shepherd, Peter Hitchcock, and John F. Scinocca. Southern Annular Mode Dynamics in Observations and Models. Part II: Eddy Feedbacks. *Journal of Climate*, 26(14):5220–5241, jul 2013.

[85] Seok-Woo Son, Sukyoung Lee, Steven B. Feldstein, and John E. Ten Hoeve. Time Scale and Feedback of Zonal-Mean-Flow Variability. *Journal of the Atmospheric Sciences*, 65(3):935–952, mar 2008.

[86] Seok-Woo Son, Neil F. Tandon, Lorenzo M. Polvani, and Darryn W. Waugh. Ozone hole and Southern Hemisphere climate change. *Geophysical Research Letters*, 36:1–5, 2009.

[87] Courtenay Strong and Gudrun Magnusdottir. Tropospheric Rossby Wave Breaking and the NAO/NAM. *Journal of the Atmospheric Sciences*, 65(9):2861–2876, 2008.

[88] Lantao Sun, Gang Chen, and Jian Lu. Sensitivities and Mechanisms of the Zonal Mean Atmospheric Circulation Response to Tropical Warming. *Journal of the Atmospheric Sciences*, 70(8):2487–2504, aug 2013.

[89] N. C. Swart and John C. Fyfe. Observed and simulated changes in the Southern Hemisphere surface westerly wind-stress. *Geophysical Research Letters*, 39(16), aug 2012.

[90] Koutarou Takaya and Hisashi Nakamura. Mechanisms of Intraseasonal Amplification of the Cold Siberian High. *Journal of the Atmospheric Sciences*, 62(12):4423–4440, 2005.

[91] Qiuhong Tang, Xuejun Zhang, Xiaohua Yang, and Jennifer a. Francis. Cold winter extremes in northern continents linked to Arctic sea ice loss. *Environ. Res. Lett. Environ. Res. Lett*, 8(8):14036–6, 2013.

[92] The Royal Society. *Ground-level ozone in the 21st century: future trends, impacts and policy implications*. Number October. 2008.

[93] David W. J. Thompson and Susan Solomon. Interpretation of recent Southern Hemisphere climate change. *Science (New York, N.Y.)*, 296(5569):895–9, may 2002.

[94] David W. J. Thompson and John M. Wallace. Annular modes in the extratropical circulation. Part I: Month-to-month variability*. *Journal of Climate*, 13(1999):1000–1016, 2000.

[95] S. Tibaldi and F Molteni. On the operational predictability of blocking. *Tellus A*, 42A(3):343–365, 1990.

[96] Kevin E. Trenberth, Aiguo Dai, Roy M. Rasmussen, and David B. Parsons. The changing character of precipitation. *Bulletin of the American Meteorological Society*, 84(9):1205–1217+1161, 2003.

[97] Gary A. Wick, Paul J. Neiman, F. Martin Ralph, and Thomas M. Hamill. Evaluation of Forecasts of the Water Vapor Signature of Atmospheric Rivers in Operational Numerical Weather Prediction Models. *Weather and Forecasting*, 28(6):1337–1352, 2013.

[98] Tim J. Woollings, Christian L. E. Franzke, D. L. R. Hodson, B. Dong, Elizabeth A. Barnes, C. C. Raible, and J. G. Pinto. Contrasting interannual and multidecadal NAO variability. *Climate Dynamics*, jul 2014.

[99] Tim J. Woollings and Brian J. Hoskins. Simultaneous Atlantic Pacific blocking and the Northern Annular Mode. *Quarterly Journal of the Royal Meteorological Society*, 1646(October):1635–1646, 2008.

[100] Jeffrey H. Yin. A consistent poleward shift of the storm tracks in simulations of 21st century climate. *Geophysical Research Letters*, 32(18):L18701, 2005.

[101] Yang Zhang, Xiu-Qun Yang, Yu Nie, and Gang Chen. Annular ModeLike Variation in a Multilayer Quasigeostrophic Model. *Journal of the Atmospheric Sciences*, 69(10):2940–2958, oct 2012.